Computational Fluid-Structure Interaction for Vocal Fold Modeling

By

Siyuan Chang

Dissertation

Submitted to the Faculty of the

Graduate School of Vanderbilt University

in partial fulfillment of the requirements

for the degree of

DOCTOR OF PHILOSOPHY

in

Mechanical Engineering

December 2016

Nashville, Tennessee

Approved:

Haoxiang Luo, Ph.D.

Bernard Rousseau, Ph.D.

Deyu Li, Ph.D.

Caglar Oskay, Ph.D.

ACKNOWLEDGEMENTS

TABLE OF CONTENTS

Chapters

LIST OF TABLES

LIST OF FIGURES

CHAPTER 1   INTRODUCTION

1.1   Background of vocal fold modeling

Voice production process, or phonation, involves aerodynamic interaction of a turbulent glottal jet flow and a pair of three-dimensional (3D) vocal folds stretched between the laryngeal cartilages. The pulsatile airflow is responsible for activating and sustaining the vocal fold vibration, and the oscillation pattern of the vocal folds in turn modulates the airflow. This dynamic interaction determines various voice characteristics (e.g., modal voice, breathiness, creakiness, and falsetto) [1]. Statistics show that approximately 7.5 million people in the United States have a type of voice disorder [2]. These disorders are debilitating and can lead to discomfort, pain, poor work performance, social withdrawal, and even long-term disability. An advanced computational model of the fluid–structure interaction (FSI) during phonation will find extremely useful applications in the medical research, diagnosis, and treatment of these disorders. For fundamental medical research, the stresses and strains in the tissue calculated from the computational model can be used to correlate with the changes observed in epithelial morphology, tissue permeability, and inflammatory gene expression, and will thus lead to new explanations for the cause of acute phonotrauma [3]. For clinical diagnosis, including the nonlinear tissue properties allows researchers to model a wide range of vocal fold dynamics including large deformations and abnormal vibrations, and computational modeling can be combined with high-speed laryngoscopic imaging techniques to analyze vibratory patterns of the vocal folds and determine the specific disease [4]. For clinical treatment, the computational modeling of phonation can be used to predict and improve the outcome of implants (e.g., medialization thyroplasty) [5], surgically altered larynges (e.g., injection laryngoplasty) [6,7],

engineered vocal fold tissues [8,9], and artificial larynges [10]. For these applications, a high-fidelity simulation tool is needed to accurately account for the time-dependent interaction between the 3D airflow and the soft tissue dynamics.

1.2   Physiology, *in vivo* study methods, and physical models

Anatomically, the vocal fold consists of a pair of soft tissue folds stretched symmetrically and horizontally across the larynx, which is located in the anterior neck below the epiglottis and above the trachea. The gap between the two folds is called glottis, which is open during breathing for air going into and out of the body. The vocal tract superior to the glottis is called the supraglottis while the inferior is subglottis. During phonation, or voice production, the vocal fold is adducted to close up the glottis, and as the subglottal pressure is above certain threshold, the glottis is forced open; but subsequently, the pressure in the glottis drops once the airflow goes through due to the Bernoulli effect and the glottis closes up again because of elastic rebound of the vocal fold tissue. Such an opening-closing cycle is thus established, which leads to sustained vocal fold vibration on order of 100 Hz and subsequent audible sound. Other than the unsteady glottal aerodynamics, vibration of the vocal fold also largely depends on the structure and material properties of the tissue. Generally, from a biomechanical perspective, the vocal fold could be divided into three major layers, from superficial to deep, i.e., the mucosa, the vocal ligament, and the underlying muscle [11]. The vocal fold mucosa is closely related to the vibratory function to produce sound. It can be further divided into the superficial layer called epithelium and the most superficial layer of the lamina propria (SLP), which is mostly composed of loosely arranged fibers of collagen and elastin. Deep to the mucosa layer is the vocal ligament, which consists of the intermediate and deep layers of the lamina propria (LLP and DLP) with increased rigidity. The vocal ligament is primarily composed of elastin and collagen that are

roughly parallel to the vocal fold edge, providing support to the vocal fold and adhesion between its multiple layers. The deepest layer among those three layers is the vocalis muscle, which is merely movable compared with mucosa vibration. Such a layered structure and inhomogeneous elastic properties affect the vocal deformation and shape of glottis for the airflow.

Previous studies on phonation and vocal fold vibration include *in vivo* measurements, *ex vivo* experiments and computational modeling. All of these methodologies have their own advantages in studying the biomechanics of the vocal fold, and together they have provided in-depth understanding of physical process of phonation.

Substantial *in vivo* measurements have been done on human and animal subjects to study phonation directly. There is a large volume of literature describing these measurements [12,13]. In general, *in vivo* experiments can yield important data regarding acoustic characteristics such as the frequency spectrum and amplitude of sound, aerodynamic quantities such as pressure and flow rate, and vibratory characteristics of the glottis through high-speed imaging approaches. These data provide critical input for modeling through either physical experiments or computational models. However, *in vivo* studies have rather limited applications in understanding details and depth of phonation, due to difficulty in instrumentation and special issues related to human and animal subjects. For example, high-speed imaging observation is limited to superior views, the medial surface and inferior region are inaccessible. Therefore, only superior side of the vocal fold deformation is visible; in addition, other details of the FSI system, such as flow field, interior tissue displacement, and stress distribution within the tissue, are all unavailable through *in vivo* experiments.

Ex vivo studies include experiments using excised larynges or physical models constructed with engineering materials. Excised larynges have main advantages over physical

models because of their actual geometric representation and tissue properties. Both human cadaver and animal laryngeal samples have been used in previous studies [14–17]. Due to the symmetry of vocal fold vibration in normal phonation, often half a larynx is used in the experiment and is attached to a transparent, solid surface. Visualization and measurements for the flow and vocal fold displacement could be performed from not only the subglottal direction but also the sagittal direction. However, excised larynges may be prone to tissue dehydration and shrinkage, which will lead to changes in the geometry and tissue properties; in addition, excised larynges are not amenable to systematic parameter studies such as the effects of size, shape, and material properties.

Physical models, especially those using synthetic materials to represent the elastic vocal fold tissue, have been developed in past few years. Both static models [18] and self-oscillating models were constructed in the experiment, which may consist of either a homogeneous material or several layer structures [19,20]. In comparison with excised larynges, these physical models could be used to systematically study the effects of geometrical and material parameters on vocal fold deformation and flow behavior, thus allowing in-depth understanding of the vocal fold dynamics.

1.3   Computational modeling for vocal fold vibrations

As an alternative method to experimental studies, computational modeling has the advantages of low cost, short completion time, providing details of information, and ability to simulate idealized situations. Therefore, computational modeling has been commonly used in engineering design as a routine predictive and optimization tool. In the context of phonation, various computational models have been created to model the interaction between the airflow and vocal fold tissue. In early stages, discrete or lumped-mass systems were created to

understand onset of phonation [21,22]. In these models, the vocal fold is simplified to two or more mass blocks connected to elastic springs, and the Bernoulli equation or other simplified flow equations are used to model the airflow. Despite its simplicity, such models can capture self-induced oscillations and have been used extensively to understand basic effects of governing parameters such as subglottal pressure and tissue stiffness, and also to investigate characteristic behavior of normal and abnormal phonation, e.g., chaotic vibration and vocal fold polyps [22].

With the development of high-performance computing hardware and software, continuum-mechanics based computational models are being increasingly used for vocal fold modeling. For example, both two-dimensional (2D) and 3D finite-element models have been developed to simulate the vocal fold deformation [23–25]. These models were used to investigate continuous and more realistic deformation of the vocal fold, vocal fold impact stress, vocal fold adduction and abduction, and other characteristics [23–25]. In addition to linear elasticity that was often assumed for mechanical behavior of the vocal fold tissue, anisotropic and inhomogeneous behaviors are sometimes also incorporated into the computational models to represent more realistic properties of the tissue.

For the FSI modeling, the finite-element model of the vocal fold needs to be coupled with a flow model. Due to the sophisticated laryngeal anatomy and high Reynolds number (around 3000 based on the flow speed, air viscosity and glottal opening), the flow is undoubtedly three-dimensional and very likely turbulent. Therefore, in FSI models, usually at least 2D viscous flows are simulated to obtain the pressure and shear stress distributions on the vocal fold surface. In some early studies, simulations were typically performed at much lower Reynolds numbers or the flow was not well resolved; so there was limited report about the vortex pattern in the flow, even though the vortex structures in the flow are believed to be very important for quality of

voice [26]. More recently, high-resolution simulations have been frequently used in the FSI modeling of the vocal fold. Previous works include Luo et al [27,28], Zheng et al [29], Thompson et al [30], Cook and Luc Mongeau et al [31] and Zhang et al [19]. Using high-performance simulation, these studies have reported the vortex structures in the flow and their interaction with the vocal fold.

As modern medical imaging technology is being rapidly advanced, internal anatomy of human bodies can be viewed with unprecedented details using noninvasive approaches such as computed tomography (CT) and magnetic resonance imaging (MRI). Such imaging modalities can provide high resolution and 3D geometry of internal space, including that of the larynx. The images generated by these techniques could be used to develop more sophisticated computational models that have much realistic representation of the anatomy. Compared with the previous computational models that are based on greatly simplified geometries (even for many continuum-based models), anatomy-based models are a significant step closer to patient-specific and high-fidelity modeling of phonation, which is eventually needed for clinical care of voices of individual patients. Some recently work, e.g., Xue et al [32] and Mittal et al [33], provide insights into the development towards such medical imaging based models of the larynx.

It is noted that only a brief summary of literature is provided here to set up the context of the present study. More details about the development and improvement of vocal fold modeling can be found in review papers of Alipour et al [34] and Mittal et al [35].

1.4   General research areas identified

As discussed earlier, a large number of studies have been devoted to development of computational modeling of vocal fold vibration, and significant advancement has been made in recent years. However, many problems remain unanswered. In particular, we have identified the

following three areas of research and we plan to address them in the current study and also in the future work: 1) modeling of the 3D unsteady glottal jet flow, 2) nonlinear deformation of the tissue during vocal fold vibration, and 3) development of high-fidelity and patient-specific models. These areas are described in the following subsections.

1.4.1   Modeling of the 3D glottal jet flow

The 3D glottal flow contains rich information about voice (e.g., frequency, loudness, noisiness, and quality), and studying the fundamental flow behavior is critical to unravel the information and to better understand the complex process of voice production. The presence of 3D vortices and turbulence in the supraglottal region has indeed been reported by a number of laboratory experiments performed using in-vitro physical models of the larynx and excised larynges. However, it is still not clear what spatial and temporal characteristics these 3D vortices have and how the characteristics are affected by the complex geometry of the larynx and also by the time-varying shape of the glottis. The lack of knowledge of the 3D vortices thus creates room for application of fine-resolution simulation of the flow via direct numerical simulations (DNS) or large eddy simulations (LES).

By more accurately simulating the vortices in the glottal flow, we will gain better understanding how these vortices affect the flow separation from the vocal fold surface and the aerodynamic pressure distribution that sustains the vocal fold vibration. In addition, the detailed flow information will provide a valuable database for the future acoustic analysis of voice. That is, the incompressible flow field (which is often assumed for FSI modeling of the vocal fold due to low Mach number of the flow) generated from the flow simulations can be supplied to an acoustics solver based on the Lighthill analogy to study the effect of the unsteady vortices on the sound field and to understand the fundamental physics of the sound generation in the larynx.

1.4.2   Nonlinear tissue deformations

There has been limited study on the role of nonlinear tissue mechanics in vocal fold vibration. Generally, nonlinearity in this problem could be caused by contact of the medial surface of the two folds, and also by large displacement and large deformation of the vocal fold tissue. Note that even though vocal fold deformation is small during normal phonation, the tissue can experience large deformation during the adduction and abduction processes where the vocal folds are either brought together and split open. In addition, active regulation of the voice may cause significant vocal fold lengthening (to increase the pitch) or excessive displacement (e.g., loud voice). Furthermore, insertion of the implant in some vocal fold surgery, e.g., medicalization thyroplasty, is intended to cause the tissue have significant displacement for proper positioning. The nonlinear material behavior intuitively should play an important role in these situations, but quantitative and rigorous studies are needed. In fact, some recent experimental work on the material properties of the vocal folds has focused on characterizing the nonlinear behaviors of the lamina propria (the mucosa and vocal ligament), including the hyperelasticity and viscoelasticity [36–38]. In our study, we are particularly interested in how the material properties affect the vibratory characteristics of the vocal folds such as the fundamental frequency and vibration patterns such as the vertical wave propagation of the so-called mucosal wave.

1.4.3   Development of high-fidelity and patient-specific models

Although modern medical imaging provides a great approach to obtain the actual 3D geometry of the larynx, research effort is still needed in order to address many issues related to how to address uncertainties in various imaging modalities and how to effectively combine the imaging process with computational modeling. The available imaging approaches can be very

different in term of spatial resolution, contrast between the tissue and the cartilages, tissue preparation procedure, artificial deformation introduced during tissue preparation, and length of scan. Therefore, when constructing a computational model, one needs to be well aware of the capabilities and limitations of the imaging approach and the specific process.

Another issue related to patient-specific modeling is that even if high-fidelity anatomy could be reconstructed, there are still other unknown modeling parameters, for example, the elastic properties of the tissue material of each individual patient that is being modeled. Therefore, either simplifying assumptions have to be made, or some parameter identification approach must be used to estimate those parameters.

Finally, model validation for patient-specific models is a challenging task, as we have to answer questions like what characteristics should be used for validation and how the quantitative information can be measured in a study that involves both phonation experiment and imaging of the larynx. To our knowledge, these issues have rarely been explored and would be worthwhile to investigate extensively.

1.5   Thesis overview

This work is focused on using computational models to investigate some of the basic questions outlined in the previous section. With the understanding that many specific studies would be needed to answer those questions completely, we point out that this work only represents a preliminary step towards understanding of 3D vocal fold vibration/glottal flow and ultimate development of an efficient, high-fidelity, and subject-specific computational tool that could be used for clinical applications.

The remaining thesis is divided into four chapters. In Chapter 2, we present a 2D study of the role of finite tissue strain in the FSI of the vocal fold; in Chapter 3, we describe the tissue

preparation approach for medical imaging of the excised rabbit larynges; in Chapter 4, we present a 3D subject-specific model and validation based on the imaging data and reconstructed larynx; in Chapter 5, we discuss a further study on nonlinear material behavior and effectiveness of a reduced-order model. It should be pointed out that materials of several chapters in this thesis are directly taken from previously publications which I have coauthored. Specifically, Chapter 2 is from "Chang, S., Tian, F-B, Luo, H., Doyle, J.F., Rousseau, B. (2013) The role of finite displacements in vocal fold modeling. *Journal of Biomechanical Engineering*. **135**(11):111008"; Chapter 3 is from "Novaleski, C.K., Kojima, T., Chang, S., Luo, H., Valenzuela, C.V., Rousseau, B. (2016) Non-stimulated rabbit phonation model: Cricothyroid approximation. *Laryngoscope*. doi: 10.1002/lary.25559"; and Chapter 4 is from "Chang, S., Novaleski, C.K., Kojima, T., Mizuta, M., Luo, H., Rousseau, B. (2015) Subject-specific computational modeling of evoked rabbit phonation. *Journal of Biomechanical Engineering*. **138**(1):011005."

CHAPTER 2   ROLE OF THE NONLINEAR MECHANICS IN VOCAL FOLD VIBRATION

2.1   Introduction

Computational modeling of vocal fold vibrations is an important tool for studying the vocal fold dynamics and the physical process of voice production. In such a tool, a vocal fold model is typically coupled with an airflow model to simulate the fluid-structure interaction (FSI) during phonation. Recently, continuum mechanics based computer models have gained popularity compared to the earlier simple but nevertheless insightful lumped-mass models, e.g., two-mass models with connective springs [21,22]. In the continuum models, the vocal fold tissue is treated as a continuously deformable medium using classical solid mechanics theory, which allows the deformations of the vocal fold to be captured in more detail. In a recent work, Alipour et al. [34] have given a broad review of computational phonation in which they discussed extensively existing modeling techniques, primary research findings, and also the validation efforts.

Among many previous studies that have developed continuum models of the vocal fold, small deformations are often assumed for the vocal fold [23,28,29]. The rationale for this assumption is that during normal phonation, the displacement of the vocal fold is on order of 1 mm, which is much smaller compared to the characteristic length of the vocal fold, which is around 1 cm [12]. Thus, the strain is only approximately 10% for normal phonation. This assumption makes the model computation very efficient since the linear elasticity theory based on small deformations involves a linear strain measure and also a linear stress–strain relationship. In some recent work, nonlinear models have been adopted for the vocal fold. For

example, Pickup and Thomson [39] and Smith and Thomson [40] used a hyperelastic Ogden tissue model in their study of the geometric effect of the laryngeal configuration on the vocal fold dynamics. As a separate line of effort, Zhang et al. [36] and Chan et al. [41] have worked on characterization of the nonlinear tissue properties and the effect of the nonlinear properties on the fundamental frequency of the vocal fold. Despite these efforts, a quantitative study on limitation of the linear assumption is still rare, especially in the context of fluid–structure interaction. Further study thus may be necessary in order to develop accurate computational models that may find clinical applications.

In solid mechanics, several sources could introduce nonlinearity into the dynamics of a structure. Typical examples include geometric nonlinearity, contact mechanics, and material nonlinearity [42]. For a general solid experiencing arbitrary deformations, sometimes even when the strain is small, the displacement and accompanying rotation of some parts of the body can be large. A classic example is a cantilever beam bent under the transverse load, where the free end of the beam can go through large displacement and rotation even if the local strain anywhere in the beam is small. Such large displacement and rotation would lead to nonlinear formulation of the strain due to the significant change to the body configuration, a term referred to as geometric nonlinearity in solid mechanics [42]. Therefore, in some cases the large displacement formulation should be used for structural analysis even when the strain is only above 5%. As mentioned earlier, the vocal fold tissue may be around or somewhat exceeding this limit during normal phonation, and thus, it would be worthwhile to investigate its geometric nonlinear effect.

Contact mechanics is involved in the vocal fold dynamics due to collision of the two folds at their medial surfaces. This effect has been included in many previous studies, e.g., Refs. [24,28,43], to investigate the impact stress on the vocal fold. Since contact mechanics is

essentially a nonlinear process and it largely depends on the local geometry of the two surfaces [44], a small error relative to the overall dimension of the vocal fold could lead to significant change in the displacement of the local contact area and, therefore, less accurate prediction of the impact stress. Furthermore, although the gap between the two vocal folds, i.e., the glottis, is small as compared to the size of the vocal folds, the airflow largely depends on the width and shape of the glottis, and the flow may in turn affect the pressure distribution on the vocal folds. However, it is not yet clear whether the error due to the small displacement assumption would increase or not in the context of nonlinear fluid-structure interaction. A careful investigation of the issues described here would provide useful information on modeling errors and, thus, be helpful for future development of accurate vocal fold models.

We emphasize that the current discussion is still within the scope of the small-strain assumption. In real situations, large deformations (and thus large strains) of the vocal fold can happen as well, for example, due to substantial local deformation, lengthening of the vocal folds, or insertion of an implant. The large strain could lead to a nonlinear stress-strain relationship, i.e., material nonlinearity as referred to in solid mechanics, and it is beyond the scope of this work.

In this work, we will use a two-dimensional larynx model to study the effect of finite displacements on the characteristics of the vocal fold vibration and those of the glottal flow. The problem formulation and the theoretical background of geometric nonlinearity will be described in Sec. 2.2. Results and discussion will be provided in Sec. 2.3. Concluding remarks will be given in Sec. 2.4.

2.2 Model description and the numerical approach

2.2.1 Model setup

The two-dimensional vocal fold model is shown in Figure 2.1, where the setup is similar to the one in Luo et al. [27]. A pair of vocal folds of identical properties are placed in a straight rectangular channel representing the passageway of the airflow. The channel length and height are L = 12 cm and H = 2 cm, respectively. The channel walls are rigid, but the vocal folds are elastic and can go through plane-strain deformations (i.e., deformation in the xy-plane only). Although the vocal fold tissue is known to be anisotropic and inhomogeneous [13], here we simplify the problem by considering an isotropic and homogeneous tissue model. The tissue properties include the density ρ_s = 1 g/cm^3, Young's modulus E = 40 kPa, and Poisson's ratio v_s = 0.3. These properties are within the ballpark of previous computational models [23,24,27].

The airflow is driven by a constant subglottal pressure P_{sub} at the inlet on the left end of the channel, and it varies from 0.5 to 0.8 kPa, and the outlet pressure P_{out} is set to be zero. The air is assumed to be Newtonian and incompressible, and its density and viscosity are, respectively, ρ_f = 0.001 g/cm^3 and μ = 2 × 10^{-4} Pa·s. The governing equations for the flow are the unsteady incompressible Navier–Stokes equations

$$\frac{\partial v_i}{\partial t} + \frac{\partial v_i v_j}{\partial x_j} = -\frac{1}{\rho_f}\frac{\partial p}{\partial x_i} + v\frac{\partial^2 v_i}{\partial x_j \partial x_j} \, , \; \frac{\partial v_i}{\partial x_i} = 0 \tag{1}$$

where v_i is the velocity component, p is the pressure, ρ_f is the density, and v is the kinematic viscosity. No-slip and no-penetration boundary conditions are imposed at the channel walls and also at the vocal fold surfaces. At the inlet and outlet, the normal shear stress is set to zero.

14
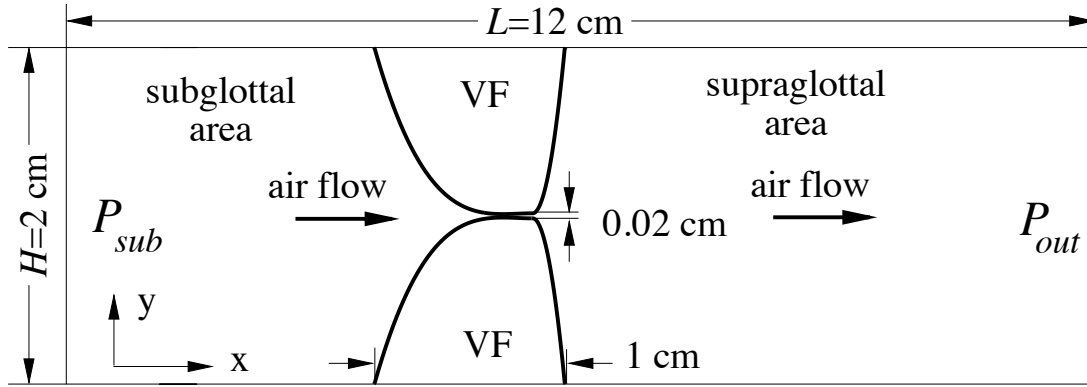
Figure 2.1 A 2D model for studying the role of geometric nonlinearity in the vocal fold dynamics

The vocal fold tissue is assumed to be governed by a linear constitutive law, which is a suitable assumption when the strain is small. However, depending on whether the solid structure experiences significant displacement and significant rotational deformations (e.g., greater than 5%), the stress and strain measures are different. Two formulations are considered here. One of them is the commonly adopted small-displacement formulation, in which the stress σ_{ij} is linearly proportional to the strain ε_{ij} by the relationship [42].

$$\sigma_{xx} = (C_{11}\varepsilon_{xx} + C_{12}\varepsilon_{yy}), \ \sigma_{yy} = (C_{12}\varepsilon_{xx} + C_{22}\varepsilon_{yy}), \ \sigma_{xy} = 2G\varepsilon_{xy} \tag{2}$$

where $G = E / (2 + 2v_s)$ is the shear modulus and C_{11}, C_{22}, and C_{12} are the elasticity constants determined from E and v_s [42]. The strain is also a linear function of the displacement, that is,

$$\varepsilon_{ij} = \frac{1}{2}\left(\frac{\partial u_i}{\partial x_j} + \frac{\partial u_j}{\partial x_i}\right) \tag{3}$$

where u_i is the displacement vector.

15

The other formulation assumes that the displacement and rotation are no longer small, and the strain measure becomes a nonlinear function of the displacement, which is termed geometric nonlinearity [12]. Using the Lagrangian formulation, the strain can be written as

$$\varepsilon_{ij} = \frac{1}{2}\left(\frac{\partial u_i}{\partial X_j} + \frac{\partial u_j}{\partial X_i} + \frac{\partial u_k}{\partial X_i}\frac{\partial u_k}{\partial X_j} \right) \tag{4}$$

where X_i refers to a material point in the reference configuration (or the undeformed state). Note that compared with Eq. (3), Eq. (4) has higher-order terms from products of the linear deformation components. Such a formulation incorporates the nonlinear effect caused by rotation of entire or part of the body, e.g., the rigid body-type rotation near the free tip of a cantilever beam when the displacement is large. In the case of vocal fold deformation, such rotational effect could happen to the vocal fold, if its cross section is viewed as a cantilever beam with the medial surface as the free end and the subglottal pressure as the load. Equation (4) also takes into account the finite deformation, if any, at the contact area during vocal fold impact. In the present work, we consider a simple material behavior, where the stress–strain formulation is the same as Eq. (2) except that the notation of the second Piola–Kirchhoff stress [42] S_{ij} would be used in place of σ_{ij}.

Henceforth, we will refer to the first formulation as model I and the second as model II. Note that the present coupled flow-vocal fold system is overall a nonlinear system no matter which constitutive law is being used. Furthermore, the contact mechanics as discussed earlier adds another source of nonlinearity to the vocal fold dynamics in both models.

2.2.2 Numerical method

The numerical simulation is performed using the fluid–structure interaction package ADINA 8.8 (ADINA R&D Inc., Watertown, MA). This finite-element package has been

previously used for vocal fold modeling [39,40,45]. A triangular mesh of 12,850 nodes and 24,576 elements is used to discretize the flow domain shown in Figure 2.1. Finer resolution is employed within the glottis and around the vocal fold surfaces. A triangular mesh of 385 nodes and 288 elements is used to discretize each vocal fold. For the transient analysis, a composite second-order method is adopted for the flow, while the Bathe integration method is chosen for the solid. The iterative solution option is chosen for the fluid-structure coupling. Descriptions of these choices can be found in the ADINA documentation. The time step is $\Delta t = 0.02$ ms, which leads to about 250 steps for a vibration cycle of approximately 5 ms. The mass-damping coefficient and the stiffness-damping coefficients are chosen to be 0.015 and 0.0002, respectively, for the vocal folds. A minimum gap of 0.2mm is assumed for the glottal gap. The two vocal folds are assumed to be in contact when they approach this specified limit. For the contact dynamics, the built-in penalty function is applied, which prevents the vocal folds from penetrating each other.

A grid convergence test is done for model II with $P_{sub} = 0.7$ kPa. In the test, the number of mesh elements is doubled, and the simulation result is compared with that from the baseline simulation. The comparison shows that the differences of the two simulations in the glottal gap width, the oscillation frequency of the vocal folds, and the impact stress (definitions of these quantities will be given later) are only 2.64%, 0.1%, and 5.69%, respectively. Therefore, the original mesh is deemed acceptable for this work. Note that as the vocal folds move, the mesh will deform correspondingly, which is done automatically in ADINA. However, manual mesh regeneration and simulation restart are necessary in some cases, e.g., $P_{sub} = 0.8$ kPa, since the mesh distortion becomes severe. To make sure that the simulations are acceptable, a similar grid convergence test was done for these cases. The result shows that after mesh refinement, the

change in the glottal gap width is less than 9% (i.e., much smaller as compared with the difference we will report between model I and model II) and the vibration behavior of the vocal fold does not vary significantly.

2.3   Results and discussions

In the current study we set the subglottal pressure P_{sub} to be 0.5, 0.6, 0.7, and 0.8 kPa. Further increase of P_{sub} would cause the mesh quality to deteriorate quickly and would require extensive manual mesh adjustment. For each value of P_{sub}, we run model I and model II separately; then, we collect the statistics after onset of the vocal fold vibration is established. The simulations were typically run for 100–200 vibration cycles, and it takes 60–100 cycles to reach steady vibration. It was determined that steady vibration has been achieved when the averaged gap width over 20 cycles does not change significantly. The statistics are collected over 20 cycles during steady vibration. We will discuss the vibration characteristics, the impact stress at the medial surfaces, and the flow behavior for each model.

2.3.1   Frequency and mode of vocal fold vibration

An eigenmode analysis is first performed for the current vocal fold model. The analysis will help us discuss the vibration pattern of the vocal folds induced by the flow. Figure 2.2 shows the lowest four eigenmodes along with the corresponding eigenfrequencies. These modes are qualitatively similar to those of a three-layer, two-dimensional vocal fold model used by Luo et al. [27]. In addition, the spectrum of the eigenfrequencies is also close to that in Luo et al. [27]. That is, the lowest frequency is near $f_1 = 100$ Hz, the second and the third frequencies f_2 and f_3 are both roughly twice that of f_1, and the fourth frequency f_4 is roughly four times that of f_1. Therefore, using the single-material model does not change the characteristics of the vocal folds qualitatively.

18
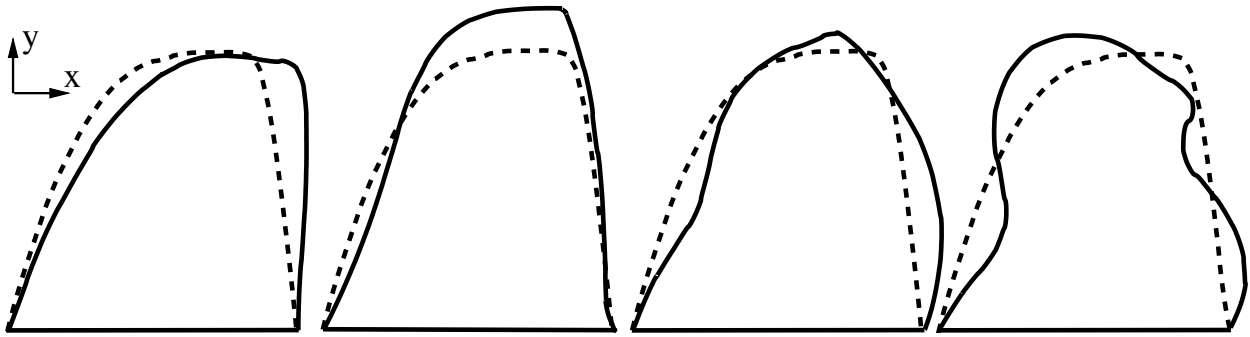
Figure 2.2 The lowest four eigenmodes of the current vocal fold model. (a) The first

mode at $f_1 = 86.9$ Hz, (b) the second mode at $f_2 = 192.2$ Hz, (c) the third mode at $f_3 = 217.5$ Hz,

and (d) the fourth mode at $f_4 = 372.9$ Hz. The dashed line is for the rest shape, and the solid line

is for deformed shape.

Figure 2.3 shows a typical time history of the glottal gap width, defined as the smallest

gap between the two vocal folds projected along the y-direction for both the transient period

(Figure 2.3(a)) and later established vibration (Figure 2.3(b)). In this figure, $P_{sub} = 0.6$ kPa and

model II is used. It can be seen that the vocal folds first oscillate at a lower frequency and then a

higher-frequency mode appears and finally takes over. A further inspection shows that these two

frequencies are, respectively, close to the first and the second eigenfrequencies. Therefore, the

current vocal folds go through a modal transition during the onset of vibration. This result is

consistent with the report in Luo et al. [28].
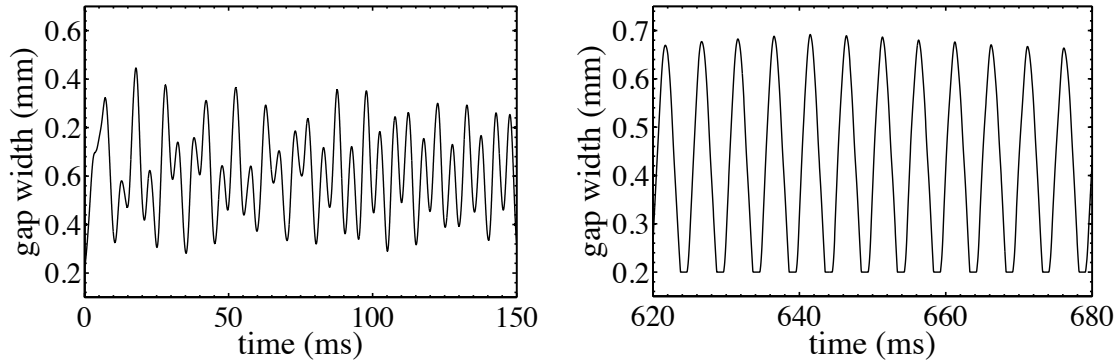
Figure 2.3 The time history of the glottal gap width for model II with $P_{sub} = 0.6$ kPa.

(a) Initial transition period and (b) the established vibration.

The dominant vibration frequency of the vocal folds during steady vibration is tabulated in Table 2.1 for both model I and model II. The frequency is calculated based on the y-displacement of a point on the medial surface (shown in Figure 2.4(a)). It can be seen that except for the case of model I at $P_{sub} = 0.8$ kPa, the frequency in all other cases is near the second eigenfrequency $f_2 = 192.2$ Hz. Furthermore, the results from model I and model II are very close to each other. However, at $P_{sub} = 0.8$ kPa the two models have significantly different results. The frequency from model II remains near f_2, but the frequency from model I is higher and is actually closer to the third eigenfrequency $f_3 = 217.5$ Hz.

Table 2.1 Dominant vibration frequency of the vocal folds as simulated using the two models

P_{sub} (kPa)	0.5	0.6	0.7	0.8
Model I: f (Hz)	201.2	201.4	203.8	220.9
Model II: f (Hz)	198.7	202.6	202.5	202.3

We further examine the vibration patterns shown in Fig. 4 for the cases of $P_{sub} = 0.6$–0.8 kPa. It can be seen that at $P_{sub} = 0.6$ and 0.7 kPa, both model I and model II produce a pattern

20

that is similar to the second mode, albeit the amplitude of vibration is greater in model II. The case with P_{sub} = 0.5 kPa, not shown here, is similar to that of P_{sub} = 0.6 kPa except that the amplitude of vibration is smaller. At P_{sub} = 0.8 kPa, the vibration from model II still has a second-mode pattern, and the amplitude becomes further increased as compared to that for P_{sub} = 0.7 kPa. However, for model I the vibration pattern at this higher subglottal pressure resembles the third eigenmode shown in Figure 2.2(c), and this result is consistent with the oscillation frequency of this case. In this particular pattern, the inlet and the exit of the glottal gap open/close alternatingly, and the maximum width of the glottis is, thus, always limited. This gap width effect will be further discussed later. To explain a plausible cause for the behavior of model I at P_{sub} = 0.8 kPa, we note that the second eigenmode and the third eigenmode of the present vocal fold model are close to each other in terms of the frequency (192.2 Hz and 217.5 Hz, respectively). Furthermore, the temporal/spatial variations of the pressure in the glottis could allow either oscillation pattern to actually take place. Therefore, the present coupled fluid-structure system may have two stable periodic orbits that are close to each other, and it could be possible that due to change of P_{sub} or system description (i.e., linear versus nonlinear strain), the system settles down to a different orbit (vibration state).
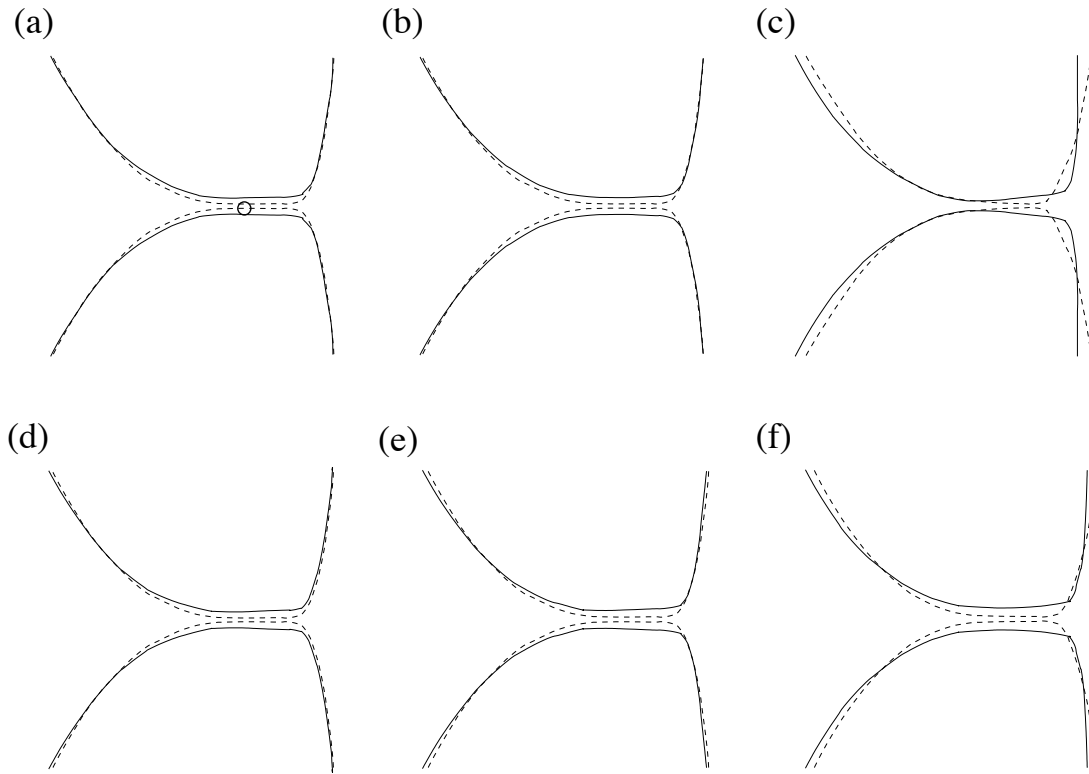
Figure 2.4 The vibration pattern of the vocal folds simulated by model I (a), (b), and (c) and model II (d), (e), and (f). The subglottal pressure is (a) and (d) P_{sub}= 0.6 kPa, (b) and (e) P_{sub} = 0.7 kPa, and (c) and (f) P_{sub} = 0.8 kPa. The solid line and dashed line represent the open and closed phases, respectively. The circle shown in (a) is the marker point that will be used in the PSD analysis.

Figure 2.5 shows the power spectrum density (PSD) analysis of the steady oscillation of the y-displacement of a point on the medial surface (shown in Figure 2.4(a)) for P_{sub} = 0.7 and 0.8 kPa. It can be seen that in all cases except model I at P_{sub} = 0.8 kPa that the power spectrum is dominated by the single frequency that is close to the second mode frequency f_2. For model I at P_{sub} = 0.8 kPa, the third mode is dominant as discussed earlier, but the second mode is also

significant. The PSD result in the cases of P_{sub} = 0.5 and 0.6 kPa is not shown here since their frequency component is similar to that in the case of P_{sub} = 0.7 kPa.
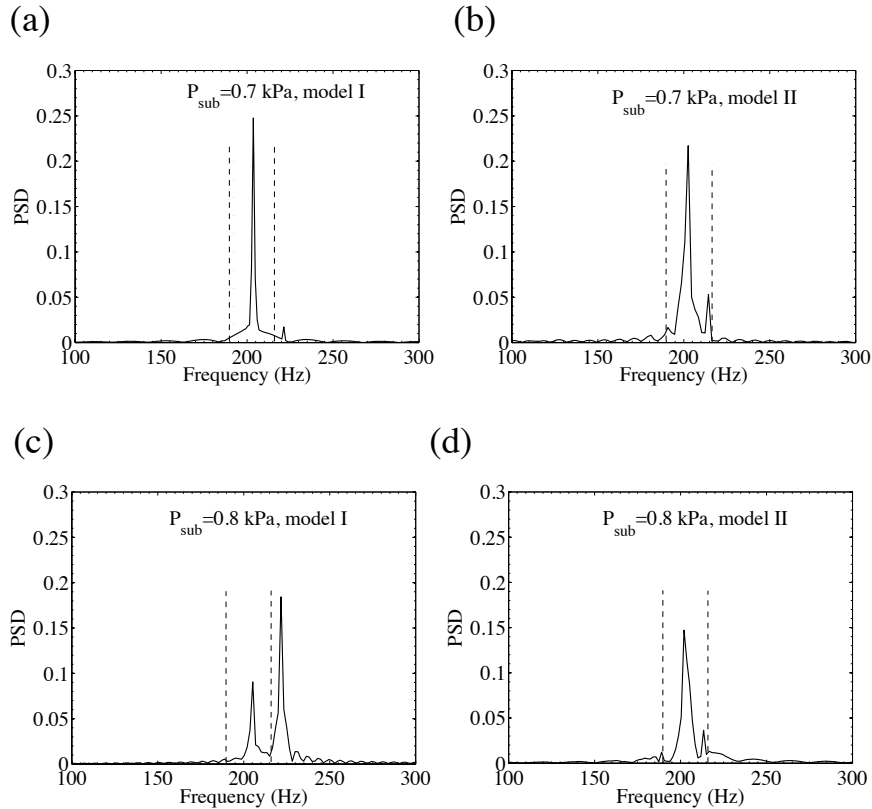
Figure 2.5 The PSD analysis of the oscillation of a point at the medial surface for P_{sub} = 0.7 and 0.8 kPa. The two dashed lines indicate the eigenfrequencies f_2 and f_3.

2.3.2 Gap width, waveform, and impact Stress

Figure 2.6(a) shows the relationship between the maximum glottal gap width and subglottal pressure for both model I and model II. In general, the glottal gap width increases when the subglottal pressure is raised, which is consistent with previous studies [13]. An exception is in the case of model I with P_{sub} = 0.8 kPa. As discussed earlier, this case has a different vibration mode that leads to a smaller gap width. The figure shows that model II

consistently gives a greater magnitude of the gap width than model I. For P_{sub} between 0.5 and

0.7 kPa, the difference between the two models is less than 0.1 mm, but it still represents about

15% of increase for model II. At P_{sub} = 0.8 kPa, the difference between the two models is clearly

large. Figure 2.6(b) shows the waveform of the gap width at P_{sub} = 0.6 kPa. We see that the

waveforms have almost the same profile for the two models since the vocal folds are vibrating at

the same mode at this pressure. However, the closed phase, or the contact time, of the vocal folds

in model II is approximately 40% longer than that of model I.
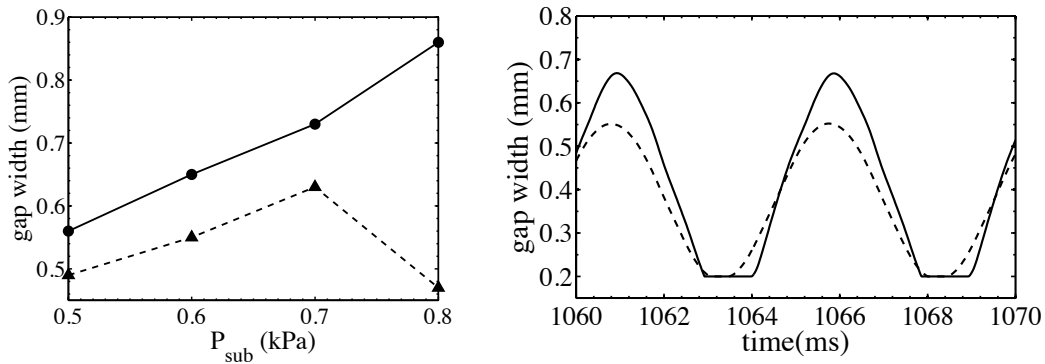
Figure 2.6 (a) The gap width during the open phase versus P_{sub}. (b) The waveform of the gap

width at P_{sub} = 0.6 kPa. In both (a) and (b), the dashed line is for model I and the solid line for

model II.

The impact stress on the medial surface of the vocal folds during collision is an important

quantity of interest, as it is likely the main contributing factor of phonotrauma [46]. Figure 2.7(a)

shows the relationship between the impact stress and the subglottal pressure. The impact stress is

calculated by averaging the stress during vocal fold collision at the contact area. At P_{sub} = 0.5

kPa, the vocal folds as predicted by model I did not reach the contact limit, and the impact stress

is thus zero. As the subglottal pressure is raised from 0.5 kPa to 0.8 kPa, the magnitude of the

impact stress is increased from 0.5 kPa to 1.5 kPa, which is generally in the data range of previous work [43].
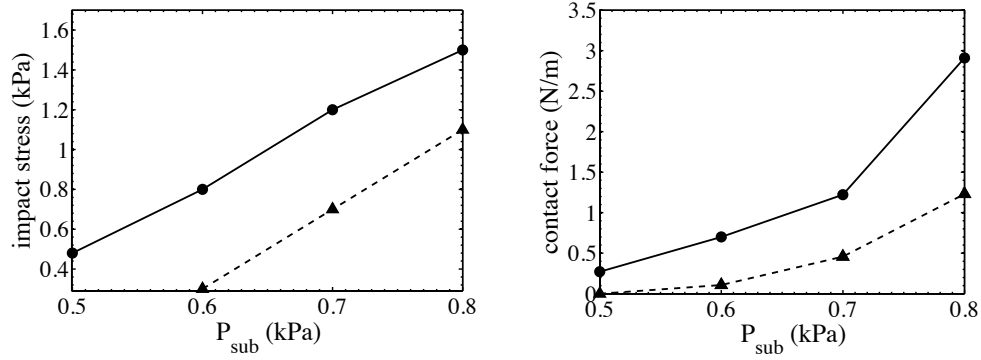
Figure 2.7 The impact stress (a) and the total contact force (per unit length in span) (b) during vocal fold collision. The dashed line is for model I and the solid line for model II.

Comparing model I and model II, we see that model II always has greater impact stress than model I, and the difference is consistently around 0.4 kPa. As greater impact also leads to a larger contact area, we also plot the total contact force per unit span in each case. The result in Figure 2.7(b) shows that the contact force increases as P_{sub} is raised, as expected. In addition, the difference between model I and model II becomes more pronounced at higher values of the subglottal pressure. At P_{sub} = 0.8 kPa, this difference is about 1.7 N/m. A further inspection shows that the locations of the maximum impact at P_{sub} = 0.8 kPa are also different between the two models. This result can be seen from the shape of the closed glottis in Figure 2.4. For model II, the greatest impact takes place in the middle of the medial surface (Figure 2.4(f)), which is also the case for the lower values of P_{sub} in Figure 2.4. For model I, Figure 2.4(c) shows that the greatest impact instead takes place near the glottal exit.

2.3.3 Flow characteristics

Figure 2.8(a) shows the flow rate Q averaged in time, from the two models. The flow rate increases nearly linearly with the subglottal pressure for model II. For model I, the flow rate is lower than that of model II for all levels of the subglottal pressure, and this result is consistent with the result comparison on the glottal gap width as discussed earlier. At $P_{sub} = 0.8$ kPa, the flow rate given by model I becomes much lower than that of model II, and this result is due to the different vibration modes in the two models as discussed earlier. In this case, $Q = 124$ cm^2/s for model II, and for model I the flow rate is only $Q = 83$ cm^2/s. From the waveform plotted in Fig. 8, the flow rate in model I not only has a lower magnitude but also has a significantly different temporal profile than that in model II.
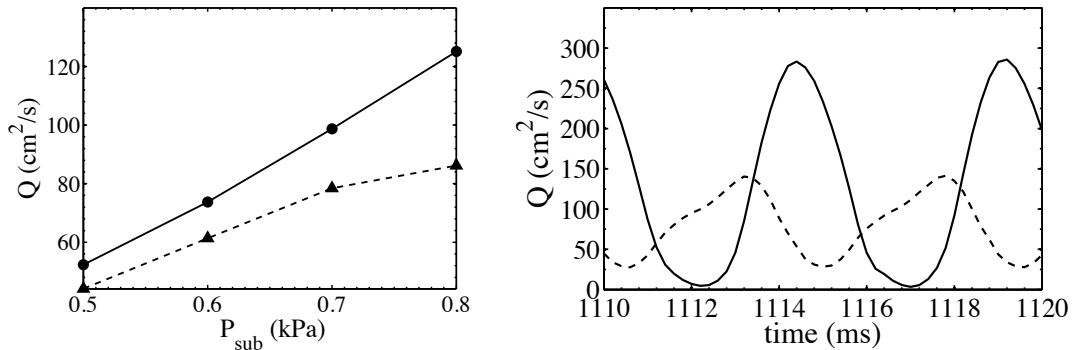
Figure 2.8 (a) The time-averaged flow rate (per unit span) and (b) the waveform of the flow rate at $P_{sub} = 0.8$ kPa. The dashed line is for model I and the solid line for model II.

The vorticity plot indicates that when P_{sub} is increased, the flow fields from models I and II become significantly different from each other. Figure 2.9 shows the comparison of the instantaneous vorticity during the maximum opening phase between the two models at $P_{sub} = 0.8$ kPa. Compared to the cases with low P_{sub}, the jet Reynolds number, defined as Re = $3Q/2v$, is

26

higher at $P_{sub} = 0.8$ kPa, and thus the flow field is more complex. In addition, at higher P_{sub}, the jet becomes more asymmetric and its skewness varies from cycle to cycle. Discussed in detail in Luo et al. [16], these phenomena are typical for the glottal airflow, and they are present in both models from the figure. However, we see that the jet is clearly stronger in model II than in model I, as in model II the jet has longer penetration length and produces stronger vortices downstream.
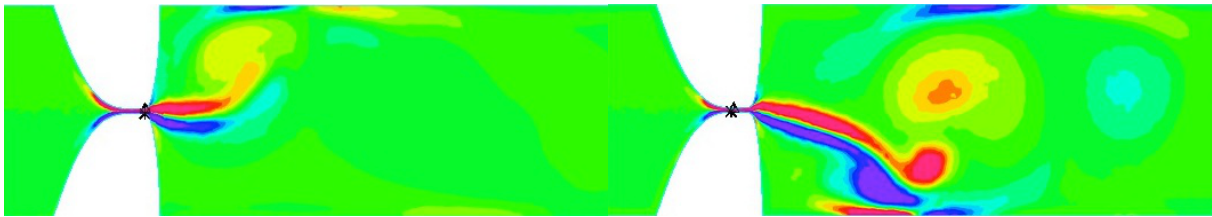
Figure 2.9 Instantaneous vorticity contours during vocal fold opening for (a) model I and (b) model II at $P_{sub} = 0.8$ kPa.

2.3.4   Further discussion

In the present study, the subglottal pressure is no greater than 0.8 kPa and is not particularly high as compared with the range of the normal phonation pressure [13], and the deformation magnitude of the vocal folds is less than 1 mm, i.e., 10% of the size of the vocal folds. However, significant differences are produced by using model II in the predicted glottal gap width, impact stress, and flow characteristics. Note that in human phonation, the displacement up to 2mm has been reported for the vocal folds [46]. To investigate the source that has caused such differences, two additional tests are introduced where the flow is assumed to be absent and the load on the vocal folds is manually specified. In the first test, a single vocal fold identical with those in the present FSI study is considered, and a uniform and static load p is applied on the subglottal and medial surfaces as shown in Figure 2.10(a). In the second test, the

load is sinusoidal with the amplitude p and the frequency at 200 Hz, and both vocal folds are present so that collision would occur. For both tests, we compare the displacement of the vocal folds calculated from model I with that from model II.
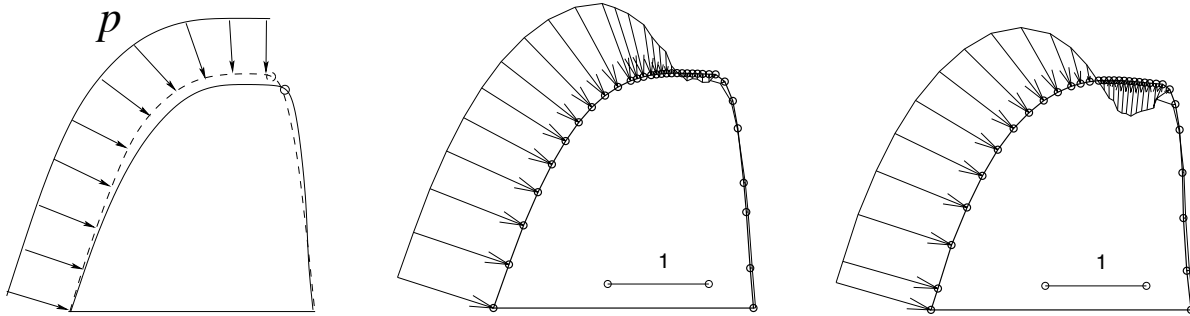
Figure 2.10 (a) Illustration of the load tests of the current vocal fold model. The reference point marked by a circle is used to measure the displacement. (b) and (c) p = P_{sub} from the FSI simulation during vocal fold opening for (b) P_{sub} = 0.6 kPa and (c) P_{sub} = 0.8 kPa.
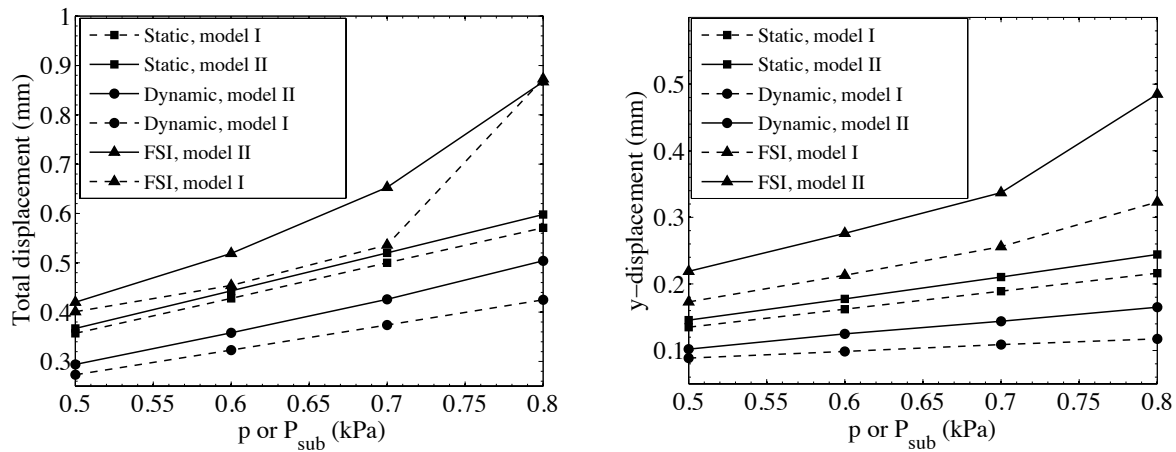
Figure 2.11 Displacement of the reference point in the static load test, the dynamic load test, and the coupled FSI simulation. (a) The total displacement and (b) the y-displacement.

Figure 2.11 shows the result from the static test and the dynamic test. For comparison, we have also included the results from the coupled vocal-fold/flow simulation. The displacement of a point at the supraglottal exit as shown in Figure 2.10 is used for such comparison. The magnitude of the load p is raised from 0.5 kPa to 0.8 kPa, to be consistent with the subglottal pressure used in the FSI simulation. Both the y-displacement and the total displacement (i.e., both x and y components included) are shown for the reason that will be explained soon.

Figure 2.11(a) shows that in the static test, the total displacement from model I is near 0.6mm at p = 0.8 kPa. Model II predicts only slightly greater deformation than model I at all load levels, and the difference is about 5% for p = 0.8 kPa. In the dynamic test, the relative difference between the two models becomes more significant than in the static test. As p is increased to 0.8 kPa, we see that the difference between the two models becomes more evident. This result can be explained since the contact of the two solid surfaces is a nonlinear function of the deformation and the difference between the two present structural models can be increased through the contact process.

When the airflow is introduced in the simulation, the total displacement of the vocal folds is in general greater than those in the no-flow tests, as shown in Figure 2.11 (a). In Figure 2.10(b) and Figure 2.10(c) we plot the pressure over the vocal fold surface normalized by P_{sub} for P_{sub} = 0.6 and 0.8 kPa. From these plots, we see that the pressure changes rapidly along the medial surface as expected. More importantly, the normalized pressure distribution in the case of P_{sub} = 0.8 kPa is significantly differently from that of P_{sub} = 0.6 kPa. This change of loading status, thus, helps to explain why the displacements shown in Figure 2.11 are not linearly proportional to P_{sub} for the FSI cases. At P_{sub} = 0.8 kPa, the total displacement is near 0.9 mm, i.e., 9% of the size of the vocal folds, for both model I and model II. This total displacement is mostly in the x-

direction due to the mean displacement of the vocal folds. The rotational effect and the coupling of the x- and y-components of deformation due to this mean displacement have been incorporated in the geometric nonlinear formulation, as discussed in Sec. 2.2.1. Since the y-component of the displacement is not necessarily linearly proportional to the x-component and the y-component is critical in determining the glottal opening, we show a comparison of this component in Figure 2.11(b). In this figure, the comparisons of model I and model II in the static and the dynamic tests are similar to those shown in Figure 2.11(a). That is, the difference between the two models is more pronounced in the dynamic test where contact is present. For the FSI simulation, the y-displacement from model I is 0.32 mm, which is significantly smaller as compared to 0.49mm from model II and represents a larger difference than in the no-flow cases. Note in both no-flow and FSI tests, the only difference between model I and model II is that geometric nonlinearity of the vocal folds is included in model II. From these test results, we see that the error due to ignoring geometric nonlinearity in modeling the vocal fold dynamics could be amplified through the interaction of the vocal folds with the flow and, consequently, lead to significant error in the prediction of the coupled system.

2.4   Conclusion

We have numerically studied the flow-induced vocal fold vibration using a two-dimensional computational model under assumption of small strains. The vocal fold tissue is assumed to be linearly elastic, but no restriction is required for its displacement and rotation so that the effect of geometric nonlinearity has been included in the model. By comparing this model with the previously commonly adopted small-displacement model (model I), we studied the effect of the finite displacement (model II) on the vocal fold dynamics and also on the glottal airflow.

The simulation result shows that model I produces consistently a smaller vibration amplitude for the subglottal pressure considered and, consequently, the impact stress and the flow rate are significantly lower than those obtained from model II. In some cases, even the vibration mode of the vocal fold predicted by model I is different from that by model II, e.g., for the subglottal pressure at 0.8 kPa in the present study. Further investigation shows that the nonlinear effect is significant when the contact process and in particular, the flow-vocal-fold interaction, are involved, both of which are sensitive to the displacement of the vocal folds.

In the case of phonation, the width and shape of the glottis are determined by the vocal fold displacement, and errors in predicting the vocal fold displacement may lead to significant change to the glottis and, therefore, to the vocal fold collision and the glottal airflow. The present study is limited to two dimensions and the isotropic/homogeneous tissue properties, and the quantitative results reported here may not be directly applicable to the vocal models in the previous studies or to the real vocal fold tissue. However, it suggests that for the sake of caution, including geometric nonlinearity in a computational model would be preferable for an accurate simulation of the vocal fold dynamics.

CHAPTER 3   EXPERIMENTAL STUDY AND IMAGING OF THE LARYNX

3.1   Introduction

Laryngeal framework surgery is considered an ideal treatment approach to avoid the risks associated with surgery directly to the vocal folds. The objective of thyroplasty surgeries is to optimize voice production through modifying phonatory positioning by altering the laryngeal cartilages. Thyroplasty procedures include four primary classifications of medialization and augmentation, lateralization, relaxation, and tensing [47]. Bilateral Isshiki type IV thyroplasty, or cricothyroid approximation, is a technique in which the thyroid cartilage and cricoid cartilage approach one another. This action results in increased vocal tension, similar to engaging the cricothyroid muscle [48]. Type IV thyroplasty is intended to increase fundamental frequency. It is a common procedure for changing the vocal pitch of male-to-female transsexual patients [49] and vocal fold paralysis [50].

Suturing *ex vivo* larynges is a useful methodological approach to refine common surgical procedures. Laryngeal suturing techniques in *ex vivo* models have examined the effectiveness of suture tension, force, and direction on medialization thyroplasty surgery [51] and arytenoid adduction [52–54]. *Ex vivo* laryngeal suturing also has significant value in modifying glottal configuration [14,17,55–58]. Alipour and Karnell [56] described a method of suturing the muscular processes of the arytenoid cartilages to adduct the vocal folds in canines. To vary the degree of ventricular gap, the researchers tensed and released sutures that were attached to the epiglottis. Khosla and colleagues [57] simulated vocal fold adduction by placing sutures through

32

the vocal processes of the arytenoid cartilages. To demonstrate the precision of this technique, the sutures were placed in the anterior-posterior and inferior-superior positions symmetrically.

Gray and Titze [59] successfully implemented sutures and clamps to evoke *in vivo* phonation using a canine model. The posterior vocal fold process was directly sutured and the arytenoid cartilages were clamped together to induce vocal fold approximation. It is observed that while Gray and Titze's [59] *in vivo* method is more representative of true vocal fold vibration, there is concern about inadvertently damaging the vocal fold tissue by directly suturing the vocal folds.

Although numerous *ex vivo* experiments have sutured the cartilages of the larynx to simulate vocal fold vibration, such techniques make it challenging to determine the precise phonatory parameters that would be obtained during *in vivo* phonation. The purpose of the present study was to describe an *in vivo* model of a bilateral Isshiki type IV thyroplasty in a rabbit. Evoked *in vivo* phonatory output was analyzed in terms of vibratory, acoustic, and aerodynamic parameters. This more natural method of suturing the laryngeal cartilages promotes minimal disruption to the intricate structures of the vocal folds.

3.2 Materials and methods

3.2.1 Animals

This study was performed in accordance with the Public Health Service Policy on Humane Care and Use of Laboratory Animals, National Institutes of Health Guide for the Care and Use of Laboratory Animals, and Animal Welfare Act (7 U.S.C. et seq.). The animal protocol was approved by the Vanderbilt University Institutional Animal Care and Use Committee. Six male New Zealand white breeder rabbits weighing 3-4 kg were used. Animals were anesthetized via intramuscular injections of ketamine (35 mg/kg), xylazine (5 mg/kg), and acepromazine

(0.75 mg/kg). To maintain anesthetic effects, ketamine (17.5 mg/kg) and acepromazine (0.375 mg/kg) were subsequently administered as needed. Heart rate, oxygen saturation level, and temperature were monitored throughout the procedure to assess state of anesthesia and general wellbeing.

3.2.2 Phonation procedure

Animals were placed on an operating platform in the supine position. To prepare for surgery, the neck was shaved from the submentum to the chest. Local anesthesia (0.2% lidocaine) was administered at the surgical site and a midline incision was made from the hyoid bone to the sternal notch to expose the larynx and trachea. A tracheostomy was then created to provide a stable airway. The trachea was transected just proximal to the sternum and the lower portion of the trachea was suspended to the sternal fascia. A 3.5 cuffed endotracheal tube (Willy Rusch GmbH, Kernen, Germany) was inserted into the upper portion of the bisected trachea and positioned 2 cm below the glottal opening. The cuff of the endotracheal tube was inflated to seal off the trachea and deliver airflow. Continuous humidified airflow was delivered to the glottis heated at 37° C using a Gilmont Instruments flowmeter (GF-8522, Barrington, IL) and Conch Therm III humidifier (Hudson, RCI, Temecula, CA). A bilateral Isshiki type IV thyroplasty [48] was performed to simulate the action of the cricothyroid muscle. The thyroid cartilage and cricoid cartilage were sutured together using 3-0 Webcryl sutures (Patterson Veterinary, Saint Paul, MN) to approximate one another. Suture placement increased tension to the vocal folds, resulting in medial movement of the arytenoid cartilages and vocal fold approximation. Tenseness of the sutures was adjusted until there was audible phonation. Figure 3.1 is an image demonstrating the *in vivo* suture placement and approximation of the thyroid and cricoid cartilages.
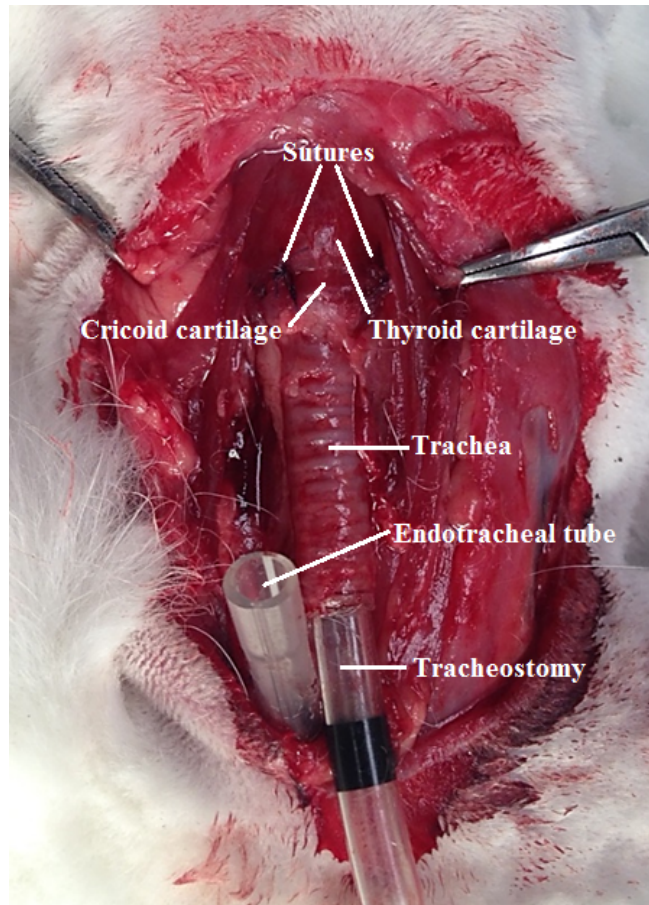
Figure 3.1 *In vivo* type IV thyroplasty. Suture placement is shown between the thyroid cartilage and cricoid cartilage on both the left and right sides to elicit vocal fold approximation. Continuous humidified airflow was delivered to the glottis through the endotracheal tube, resulting in phonation.

The larynx was suspended using an 11-cm Holinger-Tucker pediatric anterior commissure side-slotted laryngoscope (Karl Storz Endoscopy-America, Inc., El Segundo, CA). Three trials of vocal fold vibration were recorded using a 0-degree, 4.0-mm rigid endoscope coupled to a FASTCAM MC 2.1 high-speed camera (KayPENTAX, Montvale, NJ). The images were captured in black and white with 512 x 96 pixel resolution at a rate of 10,000 frames per second. To obtain acoustic measurements, three trials of phonation were recorded using a

Perception 170 Condenser microphone (AKG, Vienna, Austria) positioned 10 cm from the opening of the laryngoscope. Uninterrupted, continuous phonation was recorded for approximately 10-20 seconds. Recordings were digitized using Computerized Speech Lab Model 4500 (KayPENTAX, Montvale, NJ). The most stable 1-second portion of the acoustic waveform was selected and analyzed to obtain mean vocal intensity sound pressure level (dB) and mean fundamental frequency (Hz) values. Following acoustic analyses, sound waveforms were edited using *Cool Edit Pro* v. 2.1 (Syntrillium Software, Phoenix, AZ, 2003). To improve visualization of the waveforms, signals were amplified and excessive noise was removed. Sound spectrograms were created for spectrographic feature analysis. In addition, three trials of airflow rate (ml/s) and subglottal pressure (cm H_2O) were documented. At the end of the phonation procedure, humidified airflow was discontinued and the sutures between the thyroid and cricoidcartilages remained in place. The animals were sacrificed and larynges were harvested.

3.3   Magnetic resonance imaging procedure

Excised laryngeal specimens were secured in a 12 mL syringe with Fomblin 06/6 perfluoropolyether (Solvay Solexis, Thorofare, NJ) and placed in a 38-mm inner diameter radiofrequency coil. Scanning sequences were performed using a Varian 9.4 Tesla horizontal bore imaging system (Varian Inc., Palo Alto, CA) to obtain multislice scout images in the axial, coronal, and sagittal imaging planes. Acquired data were reconstructed using Matlab 2012a (Matworks Inc., Natick, MA) using an inverse Fourier transform. Immediately following excision, the first laryngeal sample was immersed in 10% formalin for 48 hours for tissue fixation. The sample was then transferred and soaked in 3 mM Magnevist gadolinium contrast agent (Baylor HealthCare Pharmaceuticals Inc., Wayne, NJ) in 30 mL phosphate buffer saline (PBS) for 36 hours. A 3D spin echo T2-weighted scanning sequence was used with an effective

echo time of 15 ms, repetition time of 100 ms, and a field of view of 40.96 x 22.4 x 22.4 mm.

The number of excitations was 4 and the matrix size was 512 x 320 x 320. Total scanning time

was 11 hours and 24 minutes.

3.4   Results

Suture tenseness between the thyroid and cricoid cartilages was modified until phonation

was audibly perceived. The vibratory characteristics of *in vivo* phonation were captured using

high-speed laryngeal imaging. Figure 3.2 shows a representative high-speed montage of one

cycle of rabbit vocal fold vibration that demonstrates both open and closed phases. The majority

of contact between the vocal folds occurred along the middle one-third portion. Minimal vocal

fold collision was appreciated throughout the vibratory cycles.
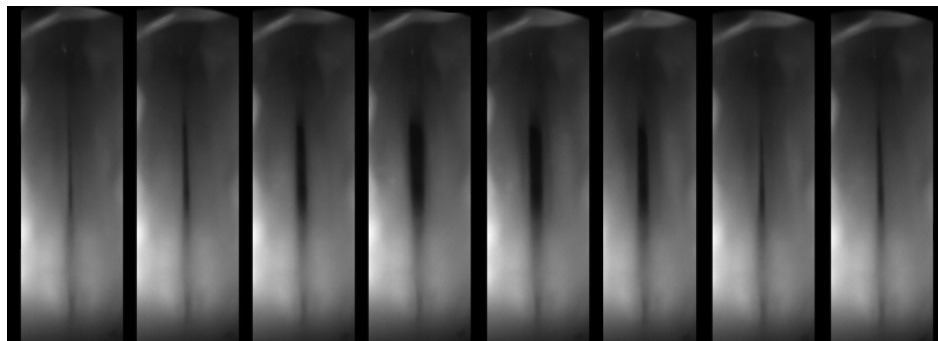
Figure 3.2 Glottal cycle montage of the closing and opening phases of vocal fold vibration using

high-speed digital imaging

Acoustic signals of rabbit phonations were recorded. One-second central portions of the

sound waveforms were selected for analysis. Across all animals, mean vocal intensity was 61.39

dB sound pressure level (*SD* = 4.03). Table 3.1 displays the means and standard deviations of

vocal intensity for individual animals across three trials. Closer examination of each trial

revealed that vocal intensity ranged between 56.15-68.52 dB. Additionally, acoustic analyses demonstrated that phonation was produced with a mean fundamental frequency of 590.25 Hz (SD = 80.79) across all animals. The range of fundamental frequency was between 419-728 Hz (Table 3.2).

Table 3.1 Mean Vocal Intensity in dB Sound Pressure Level and Standard Deviations (in Parentheses) of Rabbit Phonation across Three Trials.

Animal	Trial 1	Trial 2	Trial 3	Averaged Trials
1	59.23 (1.43)	62.20 (0.36)	61.11 (1.38)	60.85 (1.50)
2	56.76 (1.39)	58.20 (1.74)	58.60 (1.27)	57.85 (0.97)
3	64.94 (1.10)	57.65 (3.15)	…	61.30 (5.15)
4	57.91 (1.48)	56.15 (2.78)	57.26 (2.00)	57.11 (0.89)
5	65.98 (0.86)	63.32 (1.49)	63.25 (1.47)	64.18 (1.56)
6	64.83 (1.14)	68.52 (2.82)	67.78 (2.07)	67.04 (1.95)

Table 3.2 Mean Fundamental Frequency in Hz and Standard Deviations (in Parentheses) of Rabbit Phonation across Three Trials.

Animal	Trial 1	Trial 2	Trial 3	Averaged Trials
1	618.81 (4.23)	564.83 (5.87)	608.24 (1.81)	597.29 (28.61)
2	553.64 (7.94)	560.75 (7.97)	563.15 (11.50)	559.18 (4.95)
3	432.70 (10.93)	419.56 (2.65)	…	426.13 (9.29)
4	665.57 (17.30)	613.40 (92.91)	683.76 (20.06)	654.24 (36.52)
5	683.15 (11.25)	603.45 (12.52)	605.92 (12.83)	630.84 (45.32)
6	728.61 (24.14)	539.20 (179.66)	589.56 (177.67)	619.12 (98.10)

The same 1-second central portions of phonations were displayed as sound spectrograms. Spectrographic features included strong, distinctive harmonic content. Smooth, continuous variation in frequency was also observed. Lastly, aerodynamic measurements of airflow rate and subglottal pressure were documented during all trials (Table 3.3). Mean airflow rate across animals was maintained at 85.91 mL/s ($SD = 15.19$). Mean subglottal pressure was 9.00 cm H_2O ($SD = 1.54$).

Table 3.3 Mean Airflow Rate in mL/s, Mean Subglottal Pressure in cm H_2O, and Standard Deviations (in Parentheses) of Rabbit Phonation.

Animal	Mean Airflow Rate	Mean Subglottal Pressure
1	69.46 (13.48)	10.67 (1.15)
2	85.03 (0.00)	8.00 (0.00)
3	73.79 (0.00)	…
4	85.03 (0.00)	7.33 (0.58)
5	85.03 (0.00)	…
6	113.08 (0.00)	10.00 (0.00)

Following the phonation procedure and laryngeal tissue harvest, there was evidence of preservation of the adducted phonatory position of the excised larynges (Figure 3.3). Different specimen preparations and magnetic resonance scanning sequence parameters were used. Magnetic resonance scans revealed that the vocal folds remained adducted and resulted in various outcomes related to overall image resolution, contrast between tissues, and degree of tissue deformation. Figure 3.4(a) shows the first *ex vivo* larynx after the phonation procedure with sutures in place, while Figure 3.4(b) displays a magnetic resonance image of the tissue

specimen in the axial viewing plane (80 microns). It was noted that there was evidence of tissue deformation following specimen fixation in formalin solution. Tissue shrinkage was characterized by an approximately 0.5 mm glottal gap after undergoing fixation.

Figure 3.3 *Ex vivo* maintenance of vocal fold adduction. Excised laryngeal specimen is shown with sutures remaining between the thyroid cartilage and cricoid cartilage approximately 19 hours following the *in vivo* phonation procedure.
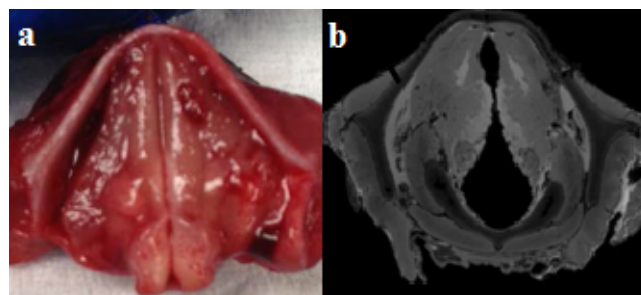
Figure 3.4 Comparison of a) *ex vivo* larynx in the adducted phonatory position and b) magnetic resonance image of the larynx in the axial viewing plane

3.5   Discussion

In the current study, we describe an *in vivo* rabbit model of a type IV thyroplasty by suturing the thyroid and cricoid cartilages together while delivering continuous airflow to the glottis to evoke phonation. *In vivo* phonation was captured using high-speed digital imaging, acoustic analysis, and aerodynamic values. Collectively, results confirm that phonation was successfully elicited using the type IV thyroplasty technique. Visual inspection of high-speed imaging indicates reduced amplitude of vocal fold vibration and only slight contact between the vocal folds. This suggests that the current thyroplasty procedure evokes vibration of lesser magnitude or stress. Acoustic analysis of rabbit phonation revealed that vocal intensity and fundamental frequency values obtained in the current study are consistent with previous results of *in vivo* modal intensity phonation using pulsed electrical stimulation to the laryngeal muscles [60,61]. Previous spectrographic analyses revealed that rabbit modal intensity phonation is characterized by strong harmonics and rare occurrences of aperiodicty [62]. Sound spectrograms of phonation in this study share similar features of this intensity of rabbit phonation. In addition, aerodynamic values of airflow rate and subglottal pressure are in congruence with expectations for modal intensity phonation in a rabbit model.

A variety of theoretical, physical, and computational models have been developed to investigate the interactions between the aerodynamic and phonatory components during vocal fold vibration [15,24,43,63–67]. In addition to providing an aid for improving surgical procedures, laryngeal modeling provides accurate details of vocal fold mechanics and enhanced insight into the study of normal and abnormal voice production. In particular, laryngeal framework surgery promotes rehabilitation of voice production without performing surgery directly on the vocal fold tissue, thus avoiding serious complications such as scarring. The

current study provides a useful method of refining one type of thyroplasty procedure, type IV, using an *in vivo* animal model.

Our laboratory's previous experiments about acute vocal fold vibration exposure were evoked via electrical stimulation to the laryngeal musculature and controlled airflow to the glottis [68]. After the larynx is excised, phonatory adduction cannot be maintained using traditional neuromuscular stimulation because there is no longer neuromuscular input to the larynx. The present study demonstrates an alternative method of eliciting *in vivo* rabbit phonation without directly suturing the vocal folds. Following the *in vivo* phonation procedure, magnetic resonance imaging revealed that the excised vocal folds maintained the adducted phonatory position.

Magnetic resonance imaging was the chosen method of scanning because of its enhanced ability to better distinguish soft tissue as compared to computer tomography imaging. Using the present technique, there can be greater examination of suture placement and tension following the experiment.

In addition to preserving vocal fold adduction during *ex vivo* imaging, the current type IV thyroplasty model has implications for future computational modeling. *In vivo* phonation can allow for precise output phonatory parameters to be quantified during computer simulations. It is noted that the *in vivo* type IV thyroplasty model may not be representative of physiologic phonation. However, the major advantage of suturing the cartilages of the larynx *in vivo* is that precise features of vocal fold vibration can be captured within the natural three-dimensional environment of a living animal.

3.6　Conclusion

　　Our current *in vivo* type IV thyroplasty rabbit model successfully sutured the thyroid and cricoid cartilages *in vivo* to elicit rabbit phonation. This method will allow for future modifications and refinements of a type IV thyroplasty with increased accuracy regarding phonatory output. This technique promotes the preservation of the vocal folds in the adducted phonatory position after excision, which may be a useful approach for future laryngeal microimaging and modeling experiments.

CHAPTER 4   SUBJECT-SPECIFIC MODELING OF THE VOCAL FOLD VIBRATION

4.1   Introduction

Vocal fold vibration during voice production is a result of biomechanical fluid–structure interaction (FSI) between the glottal airflow and the elastic tissue of a pair of vocal folds. Computational modeling of this interaction is useful for understanding the physics of voice, studying vocal fold pathology (e.g., nodules and polyps), and developing computer-based tools for clinical management of voice disorders [35,69]. In recent years, there have been significant efforts in developing advanced computational models of the vocal folds, which are driven by the rapid growth of computing power and also by the need for higher realism when one is trying to capture the features of the vocal fold dynamics for individual patients. For a comprehensive review of progress in vocal fold modeling, readers are referred to a recent article by Mittal et al. [35].

In general, a computational model for FSI of the vocal folds includes a flow model based on the viscous Navier–Stokes equation for the unsteady glottal aerodynamics and a solid mechanics model for dynamic deformation of the soft tissue. Previously, both 1D and two-dimensional (2D) models have been extensively used in the literature [27,43,70]. More expensive 3D models are also being increasingly adopted, and they may include 3D characteristics of the airflow, the tissue, or both [23,25,71–73] and can thus provide more details of the phonation process, e.g., the impact stress on the medial surface.

With assistance from modern medical imaging technology, such as computerized tomography (CT), the information on the 3D anatomy of the larynx can be obtained and

incorporated into these computational models [33]. For example, Xue et al. [32] developed a subject-specific model of human phonation based on CT scans and discussed the influence of the anterior–posterior asymmetry on the phonation characteristics along with some interesting 3D flow features. Because the CT scan did not provide morphology of the interior tissue, the internal structure of the vocal fold in their study was based on histological data, and detailed comparison between simulation and subject-specific experimental results was not provided.

In terms of cost, the 3D models are usually computationally intensive and may require days of simulation or even longer on high-performance computers. Therefore, there are rare attempts for using such models for extensive exploration in large parameter spaces. Such exploration may be needed for design optimization and for determining unknown model parameters by solving an inverse problem. As one specific example, in the computational models that are based on medical images, one typically has to assume population-averaged material properties for the tissue, even if the individual 3D morphological features can be incorporated into the model. The unavailability of individual material characteristics thus limits realism of a subject-specific model. Generally speaking, how to incorporate specific tissue properties, validation of individual-specific vibratory characteristics, and reducing the computational cost will be three of the major challenges for subject-specific models.

In this work, we investigate the feasibility of developing subject-specific models based on MR images of the rabbit's larynx and explore the use of a low-dimensional flow model to assist with identifying the elastic properties of the vocal fold tissues, by matching the simulated vibratory characteristics, with those obtained from individuals during the phonation experiment. We expect that both the method of parameter identification and the method of validation will be

45

instrumental for future development of 3D high-fidelity computational models with validated subject-specific characteristics.

4.2   Materials and methods

4.2.1   *In vivo* rabbit phonation procedure

The animal protocol was approved by the Vanderbilt University Institutional Animal Care and Use Committee. Five male New Zealand white breeder rabbits were used. As previously described [68,74], rabbit phonation was elicited by performing a bilateral Isshiki type IV thyroplasty. The procedure entailed suturing the thyroid and cricoid cartilages, thus bringing together the vocal folds, while delivering continuous humidified airflow to the glottis. In setting the sutured adduction, suture tension was adjusted for each animal until audible phonation was produced [75]. This technique promotes the maintenance of the vocal folds in the adducted phonatory position for later microimaging. *In vivo* phonation was captured using a high-speed camera (KayPENTAX, Montvale, NJ) filming at 10,000 frames per second, and the acoustic and aerodynamic measurements were performed, including measurements of the subglottal pressure, the volume flow rate, and acoustic intensity. Details of the experimental setup and data collection can be found in Novaleski et al. [75] and Ge et al. [68], which provide methodological details and schematics of the experimental setup. The subglottal pressure will later serve as an input parameter for the computer model.

To minimize the degree of vocal fold tissue change, phonation trials were elicited for only brief periods (i.e., 10–20 s per trial). These short durations were interspersed with rest periods in between each trial, until all data were collected, to control for the influence of external factors, such as changes in hydration, humidity, and other environmental effects. Presented in detail elsewhere [75], the data collected from trial to trial were fairly consistent.

4.2.2   Scanning procedure

After the phonation procedure, the larynx was excised and high-resolution MR imaging was performed to obtain details of the morphology of the vocal folds in the adducted phonatory position. These subject-specific scans were then used to accurately replicate the individual rabbit's laryngeal anatomy. Excised laryngeal specimens were secured in a 12mL syringe with Fomblin 06/6 perfluoropolyether (Solvay Solexis, Thorofare, NJ) and placed in a 38-mm inner diameter radiofrequency coil. The specimen was not doped in contrast agent and was scanned within several minutes after harvest. A magnetization-prepared and rapid gradient-echo imaging sequence was used with T2-weighted-prep with echo train length of 40, repetition time of 550 ms, and a field of view of $32\times17\times17$ mm^3. The matrix size was $512\times256\times256$. Total scanning time was 12 hrs. A Varian 9.4 T horizontal bore imaging system (Varian Inc., Palo Alto, CA) was used in the sequence to obtain multislice scout images in the axial, coronal, and sagittal imaging planes. Acquired data were reconstructed in MATLAB 2012a (MathWorks Inc., Natick, MA) using an inverse Fourier transform. We have not yet performed scanning of the *in vivo* sutured geometry.

4.2.3   Model reconstruction

The laryngeal architecture was reconstructed using manual segmentation. Based on the reconstructed larynx, a 3D computer model was generated to simulate the flow-induced vibration of the vocal folds. Figure 4.1 shows the workflow of reconstructing the laryngeal model from the MR images. The rabbit larynx was extracted from the MR scans as a surface mesh using the open-source software ITK-SNAP. The larynx included the true vocal folds, the false vocal folds, and a short segment of the trachea and supraglottal area. Manual segmentation was used here to ensure accuracy of the reconstructed geometry. The segmentation procedure was repeated by a

second experimenter to ensure its reliability. The extracted surface mesh originally had a stair-step shape but was smoothed in ITK-SNAP with Gaussian image smoothing using standard deviation of 2.0 and approximate max error of 0.02. Then, a tetrahedral mesh for finite-element analysis was generated using commercial software (ANSYS ICEM, version 13.0). The reconstructed laryngeal geometry was approximately 1.0 cm long, 1.0 cm wide, and 1.0 cm high and contained around 10,000 vertex nodes and 40,000 elements. Figure 4.2 shows the reconstructed larynx from the posterior and superior views. In the finite-element model, all the exterior surfaces are fixed except that the lumen surface is free. Because the cover layer of the vocal fold is very thin (two elements at some locations), its geometric specification could be mesh-sensitive. Thus, we manually made the larynx model and its meshing symmetric. This treatment did not create any significant problems, since the actual vocal fold vibration was fairly symmetric, as observed in the high-speed video recordings.
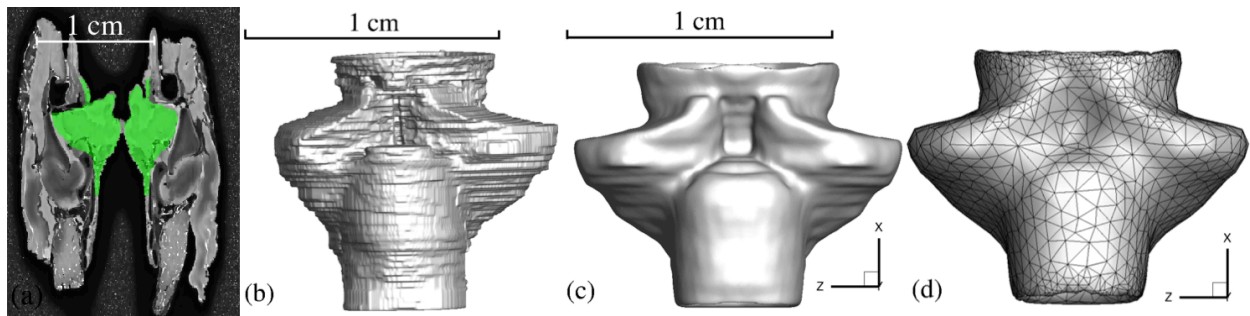
Figure 4.1 Workflow of model reconstruction: (a) segmentation, (b) surface mesh extraction, (c) mesh smoothing, and (d) the finite-element mesh

The vocal fold tissue was assumed to be isotropic and governed by the Saint Venant–Kirchhoff model with the density ρ_s = 1000 kg/m^3 and Poisson's ratio of 0.3. The Saint Venant–Kirchhoff is a simplified nonlinear model which assumes a linear relationship between the stress

and the strain but the finite strain takes into account the nonlinear effects due to large displacements and large rotation, i.e., geometric nonlinearity as previously discussed for vocal fold modeling [67,72].
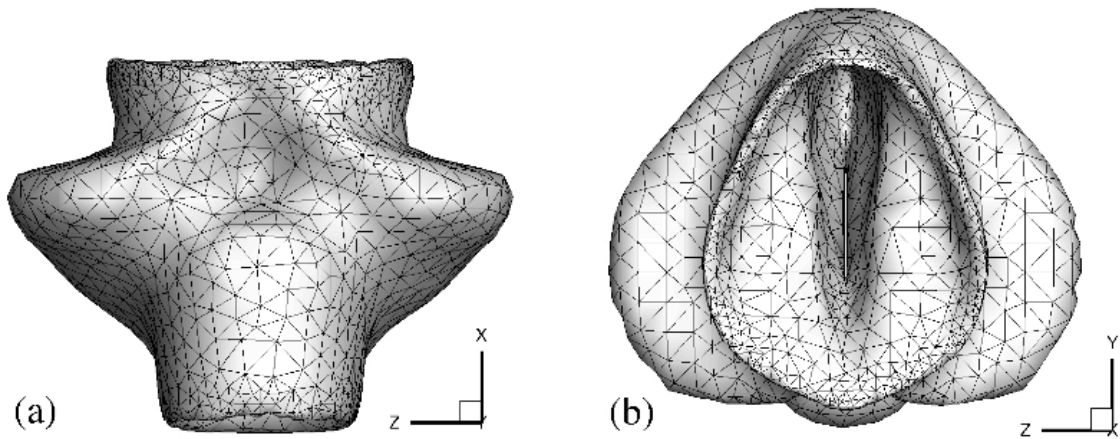
Figure 4.2 Reconstructed larynx geometry from (a) a posterior view and (b) a superior view, where the vocal fold remains in a closed position.

Approximately two layers of the internal structure of the vocal fold tissues were observed as shown in Figure 4.3(a), and thus the vocal folds were modeled to have a two-layered setup as shown in Figure 4.3(b), i.e., the vocal fold cover in contact with the air and the body underneath the cover. Such a simplified structure has also been adopted in previously studied idealized vocal fold models [23,76]. Young's modulus of each layer was later determined from the simulations. From previous measurements of the tissue stiffness for the human vocal fold, the body layer is much stiffer than the cover layer. Furthermore, the effect of the body-cover stiffness ratio has been investigated previously [76]. From these results, the ratio was kept above five in the current simulations. The thickness of the cover layer, h_c, is around 1 mm. Note that in Figure 4.3, the

view is along the x-direction and the slice is not exactly parallel with the vocal fold (see Figure 4.4 for the orientation of the vocal fold). Therefore, the cover layer is not as posterior as it appears to be in Figure 4.3.
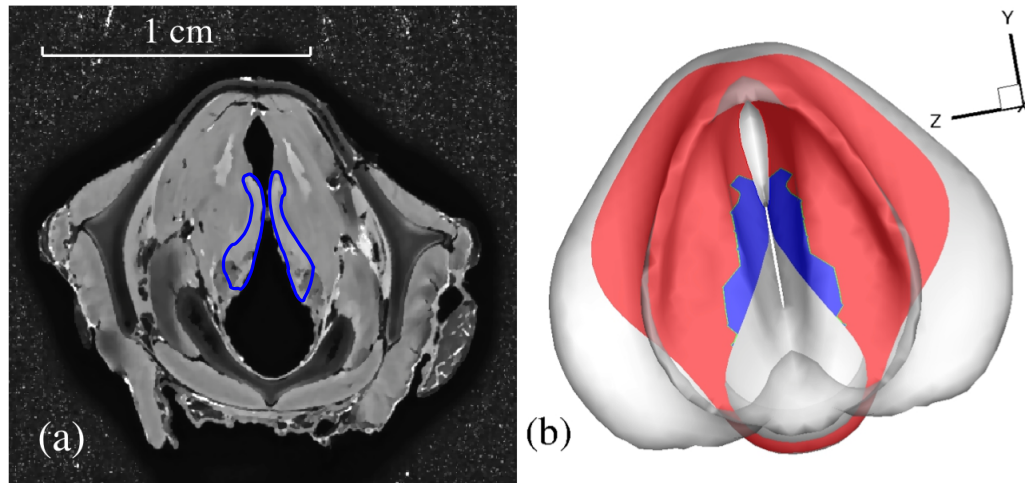
Figure 4.3 (a) An axial slice of the vocal fold from the MR scan, where the cover layer is marked out, and (b) assumption of the profile of the vocal fold cover and body in the model.

4.2.4 Setup of the hybrid FSI model.

The low-dimensional flow model in the current study is simply based on the Bernoulli principle of ideal flow. Nevertheless, when applying this principle, we will identify a proper streamline for the anatomical geometry through a 3D flow simulation of the stationary domain. Note that the Bernoulli principle has long been used as a simple tool by the voice community to study vocal fold function [12]. Previously, this 1D flow model was also combined with vocal fold models of higher dimensions (2D or 3D) to study the FSI of phonation and was shown to be capable of capturing the most basic characteristics of vocal fold vibration [19,45].

Extending the lumen surface of the reconstructed vocal fold in both subglottal and supraglottal directions as shown in Figure 4.4, we obtain an approximate domain for the airflow,

which is driven by the subglottal pressure at the inlet. To identify a proper streamline in the curved passage, the vocal fold deformation is first simulated in the absence of flow but under a constant pressure load on the tissue surface. Then, the stationary geometry with an open vocal fold was used to simulate the 3D flow through the glottis using an in-house code. Note that the magnitude of the vocal fold opening and the detailed variation in the glottal shape along the flow do not significantly affect the direction of the streamline before the glottal exit. A segment of the streamline was taken from the center of the glottis and was used for subsequent application of the Bernoulli equation. The equation and the continuity equation are

$$P_0 + \frac{1}{2}\rho u_0^2 = P_1 + \frac{1}{2}\rho u_1^2 = P_s + \frac{1}{2}\rho u_s^2$$

$$u_0 A_0 = u_1 A_1 = u_s A_s \tag{5}$$

where P, u, and A represent the pressure, the velocity, and the area of the cross section, respectively, and the subscripts represent the location of evaluation, i.e., 0 for the start of the streamline, 1 for the end where the flow separation takes place, and s for an arbitrary point on the arc in between. P_0 is assumed to be the constant subglottal pressure measured from the phonation experiment, and $P_1 = 0$ is simply the ambient pressure. The area of the cross section at any given point s will be calculated in the hybrid FSI model, based on the time-dependent deformation of the vocal folds.
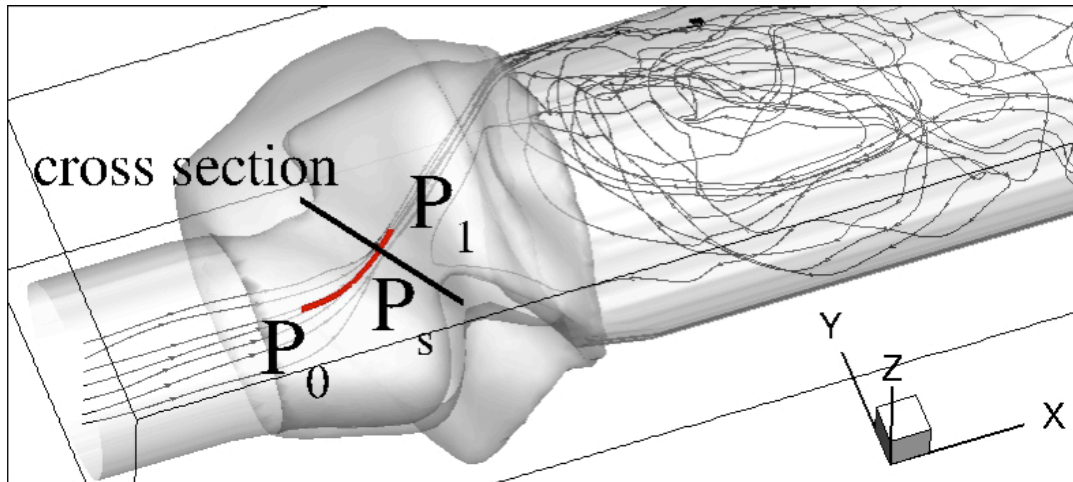
Figure 4.4 Three-dimensional flow simulation in the stationary domain with an open glottis, where the thick curved line indicates the streamline extracted for later 1D flow model and the thick straight line represents a cross section perpendicular to the streamline.

Decker and Thomson [45] reported that the influence of position of the flow separation point on the vibration frequency and displacements was small. In the current model, the separation point was consistently selected as the location with the minimum cross section area, Amin. We have tested sensitivity of the model to the flow separation point. If this location is near the minimum cross section area, then the vocal fold vibration is not significantly affected. For example, we have moved the separation point further downstream at A_1/A_{min} = 1.1, and the vibration amplitude only changes by 3% and the frequency by 1%. However, if we fixed the location at any particular point rather than keeping it dynamically varying, the change in the vibration could become more evident (e.g., significantly reduced amplitude).

The FSI simulations are performed using an in-house finite element code for soft tissue deformations [72]. The time step was 0.001 ms, and one vibration cycle took about 2000 time steps. A small gap of 0.05mm was imposed between the two medial surfaces, at which the

52

surfaces are assumed to be in contact. More than 20 vibration cycles were simulated after the vibration was well established, and from these cycles statistics were taken.

4.3   Results

4.3.1   Experimental results

As mentioned earlier, *in vivo* phonation was captured using high-speed imaging and acoustic and aerodynamic measurements. Figure 4.5 displays images from the high-speed video recordings for one typical vibration cycle of sample 1. In this figure, we also illustrate the definition of the vocal fold length, L, which begins from the anterior commissure and ends at the vocal process. From the imaging sequences, sustained vibration was observed for all samples and the opening closing motion was fairly consistent among the samples. The vocal folds move mostly in the lateral direction. However, the phase differences in the longitudinal direction and also in the inferior–superior direction can be observed.
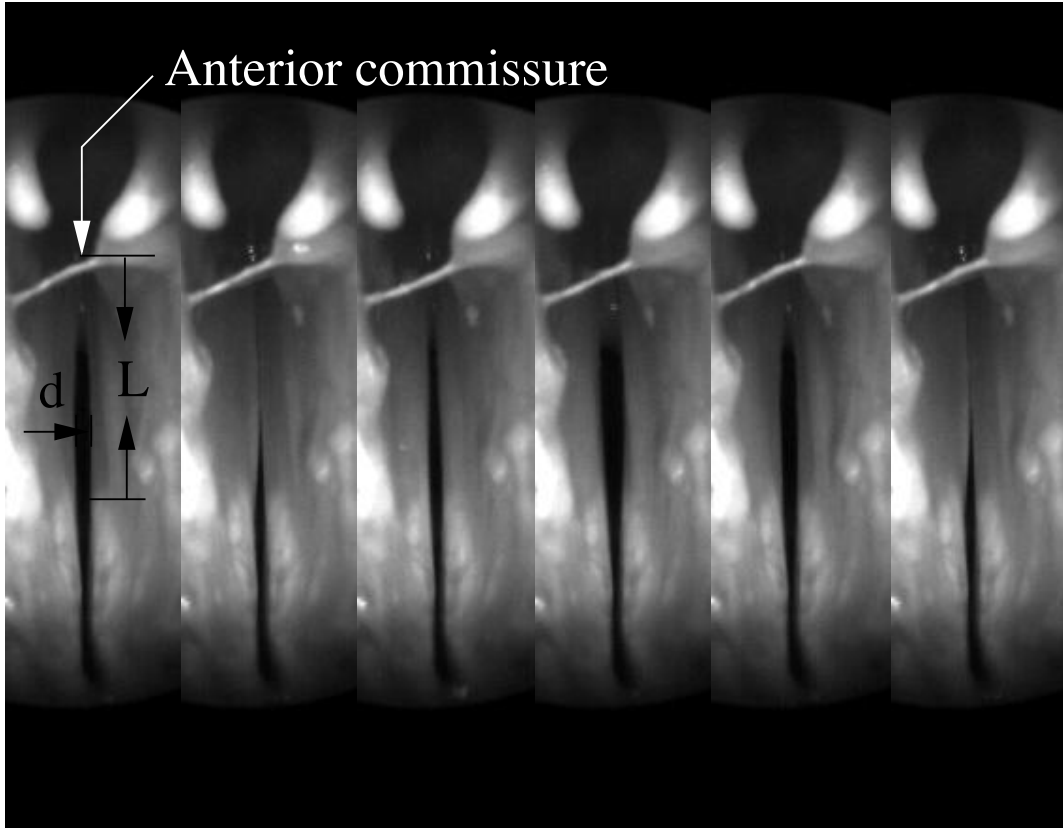
Figure 4.5 A typical vibration cycle in the evoked rabbit phonation via high-speed imaging, where the definition of vocal fold length, *L*, and the amplitude of opening, *d*, are shown.

The time-dependent vibration amplitude at the midportion of the glottis was extracted in MATLAB using its image processing toolbox, and its peak value averaged from multiple vibration cycles, d_{max}, will be used later to compare with the simulation results. Table 4.1 lists the *in vivo* aerodynamic and acoustic measurements for each sample. We point out that the phonation frequency and intensity values are similar to those obtained from experimentally induced phonation using neuromuscular stimulation (rather than suture) [74,75]. Such aerodynamic and acoustic assessment confirms that the current elicited phonations are consistent with previous modal intensity phonation and that the suture tension was appropriate.

Table 4.1 Aerodynamic and acoustic measures with the subglottal pressure P_0 (kPa), the volume

flow rate of air, Q (cm^3/s), the fundamental frequency of vibration (Hz), the acoustic intensity

(dB), and the ratio between the vibration amplitude and the vocal fold length, d_{max}/L

Sample	P_0	Q	Frequency	Intensity	d_{max}/L
1	1.05	33	564~618	59.2~62.6	0.088
2	0.78	40	553~563	56.7~58.6	0.081
3	0.72	40	419~432	56.1~57.9	0.098
4	1.00	40	613~683	63.2~65.9	0.076
5	0.98	50	539~728	64.8~68.5	0.081

4.3.2 Simulation results

The hybrid FSI model was constructed from the reconstructed 3D vocal fold tissue structure and the simplified 1D flow model as described in Sec. 4.2.4. Since the elastic properties of specific tissue samples are a priori unknown, in this study we adopted a trial-and-error approach. Note that an automated approach by solving an optimization problem is also possible but is not adopted here since the number of samples and the parameter space are relatively small in this exploratory study.

Young's modulus of each vocal fold layer was first chosen based on an eigenmode analysis of the vocal fold tissues, and a sequence of simulations of the hybrid model was then run with the goal of matching the normalized vibration amplitude, d_{max}/L, and the fundamental frequency with the experimental data listed in Table 4.1. Between 10 and 50 simulations were usually enough for each sample. The final result from the simulations is listed in Table 4.2. In the previous work of Thibeault et al. [77] and Rousseau et al. [78], the shear modulus of the rabbit

vocal fold lamina propria (within the cover layer) is between 0.2 and 20 kPa. Latifi et al. [79] later did uniaxial tensile testing of rabbit vocal fold tissues in the longitudinal direction and determined that Young's modulus is up to 170 kPa, a result that needs to be further confirmed according to them. In the current study, the vocal fold is assumed to be isotropic; thus, the stiffness becomes higher when matching the frequency with that of the anisotropic tissue, which has greater stiffness in the longitudinal direction. Nevertheless, the Young's modulus we obtained, around 10 kPa for the cover layer, still has the same order of magnitude as measured in Thibeault et al. [77] and Rousseau et al. [78].

Table 4.2 Final result from the FSI simulation including Young's modulus of the vocal fold body, E_b (kPa), Young's modulus of the cover, E_c (kPa), the normalized vibration amplitude, and the vibration frequency (Hz)

Sample	E_b	E_c	d_{max}/L	Frequency
1	60	12	0.0719	601
2	80	8	0.0851	545
3	80	8	0.0836	611
4	90	9	0.0675	589
5	90	9	0.0848	591

Comparison of the simulation and experimental results is shown in Figure 4.6 for the vibration frequency and amplitude. It can be seen from these results that in general, the vibration frequency from the model falls within the range of measured frequency, even though the model frequency is slightly lower. In Decker and Thomson [45], the frequency obtained from a similar hybrid model (where the vocal fold geometry is idealized) is about 6% lower compared with the

full 3D model. Therefore, we expect that the frequency match will be better in full 3D FSI models, developed later based on this work.
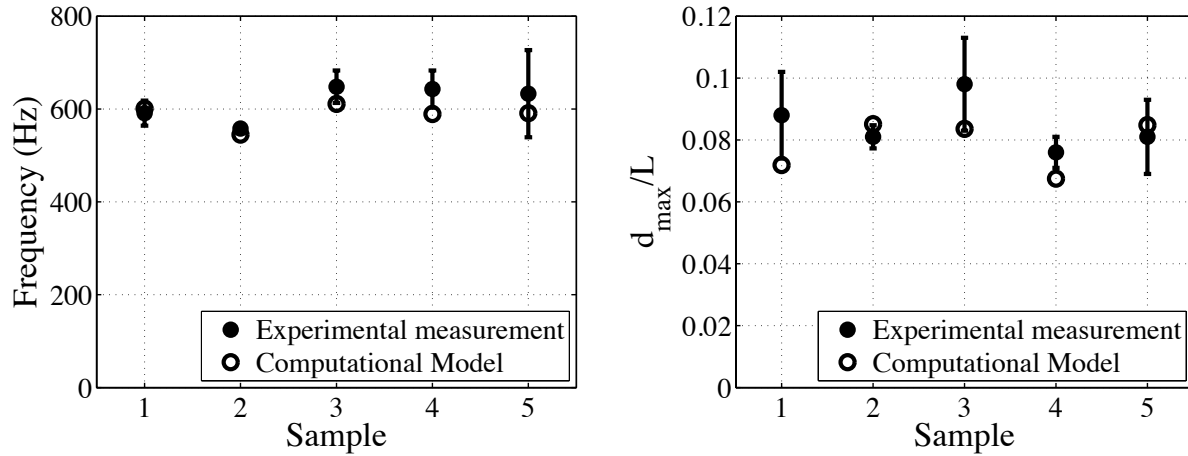
Figure 4.6 Comparison between the simulation result and experimental measurement: a) frequency; b) amplitude-to-length ratio, d_{max}/L.

The figure also shows that the normalized vibration amplitude is generally in the range of experimental results, although for samples 1, 3 and 4, the simulation gives an overall smaller amplitude.

Self-sustained vibration is established in all final simulation cases. Figure 4.7 shows typical sequences of oscillations of the glottal gap width from the experimental and model simulation. The gap width has been normalized by its averaged peak magnitude so that we can focus on the waveform only. The time is also shifted by a constant offset for easier comparison. It can be seen that the waveform obtained by the simulation matches that from the experiment reasonably well.
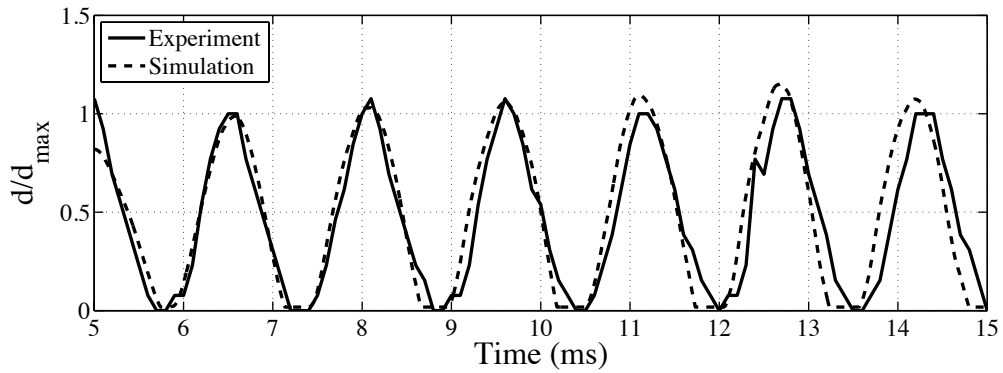
Figure 4.7 Waveform of the normalized glottal gap width from the experiment and simulation.

In Figure 4.8, one typical vibration cycle is shown for the superior view of the glottis. It can be seen that the narrow opening of the glottis generally is consistent to that observed in the high-speed video recordings. As observed in the experiment, the simulated glottis has greatest opening amplitude and greatest impact around the midportion of the medial surface.
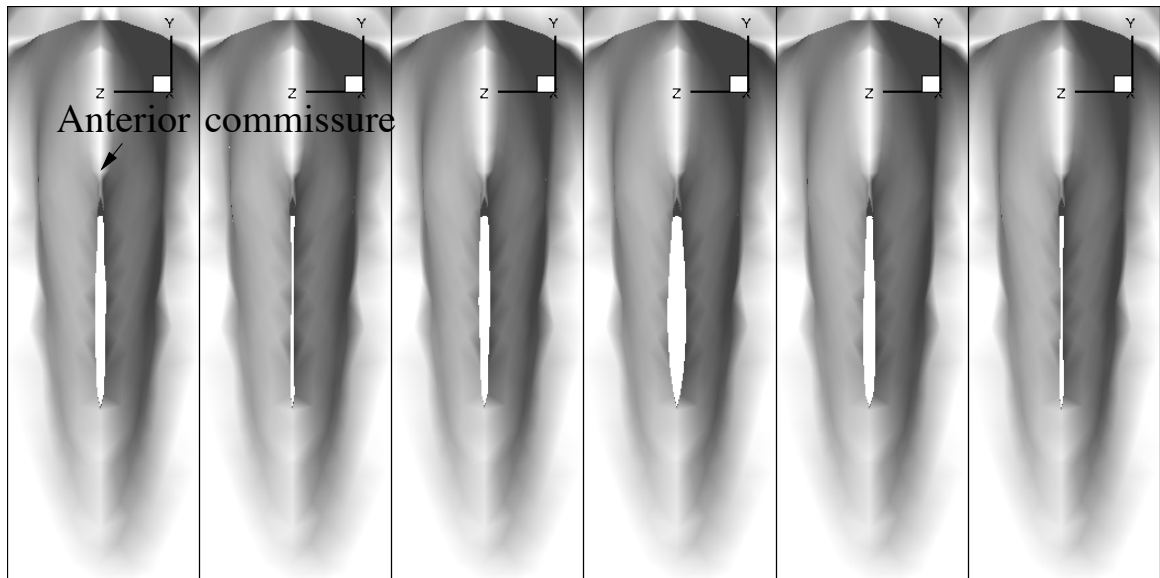
Figure 4.8 A typical cycle of vibration obtained from the simulation for Sample 1. The

anterior side is at the top in each panel.

4.4 Further discussion

The current study only represents an exploratory step toward developing future subject-specific computational models of phonation, and we focus on identification of unknown model parameters, and comparison of individual-specific characteristics between the model and subject. Both the number of subjects and number of unknown parameters in the model are very small. However, the result has implications to broader and more extensive study in the same direction. For example, the current model could be extended in a straightforward manner to incorporate an anisotropic tissue model [23] or hyperelastic materials [36]. Furthermore, a suite of well-established optimization packages could be adopted to automate the procedure. We emphasize that in this parameter identification process, reduced-order models such as in the current study will be useful tools for rapid model-based predictions and for complementary analyses along with full 3D models.

We envision that the general methodology developed in this work could be extended to the study of individual human subjects, e.g., to determine the tissue properties of the vocal fold *in vivo* and to develop corresponding 3D FSI models. However, there are several challenges in performing similar studies for live human subjects. In particular, the suture method cannot be used. Thus, performing *in vivo* high-resolution MR scanning in humans would require the development of a subject-specific task (e.g., Valsalva) that can be accomplished during the imaging procedure to overcome these challenges. Alternative imaging modalities (e.g., CT) may also be explored in future studies and used to validate the computational models generated.

Due to the simple model adopted here, the current study is also subject to some limitations. First, an isotropic tissue representation has been used with a simple constitutive law (the Saint Venant–Kirchhoff model). Second, the flow model is based on the Bernoulli principle

and thus does not provide any information on vortex formation or 3D flow pattern in the supraglottal region. This model will need to be refined for study of vibration asymmetry, where the flow may become skewed and the flow separation point will be different on the medial surfaces of the two vocal folds. Future studies using experimental and 3D computational approaches are planned to advance the accuracy of such reduced-order models.

Finally, another limitation of the current approach is that the criteria used for model validation are still limited to the most basic temporal and spatial variables. As the tissue model becomes more realistic and 3D flow is included in the full simulation, we plan to collect additional details of the vibratory characteristics and pursue higher levels of validation.

4.5   Conclusion

A combined experimental and numerical study has been performed for evoked rabbit phonation with the goal of exploring issues related to parameterization and validation of subject-specific computational models. In the present study, the laryngeal anatomy was successfully reconstructed using MR scans. An efficient hybrid model was then created to identify the unknown properties of the 3D vocal fold tissue, and the model validation was based on comparison of individual-specific characteristics of vocal fold vibration measured from the *in vivo* phonation experiment.

The results show that the models with identified parameters were able to match the vibration frequency and magnitude of individual samples. These models will be used for future study of full 3D models.

CHAPTER 5   COMPARISON OF THE REDUCED-ORDER MODEL AND THE FULL 3D MODEL

5.1   Introduction

In Chapter 4, a reduced-order FSI model that couples a one-dimensional flow model with the 3D anatomical vocal fold model based medical imaging data was utilized to describe the FSI process of the vocal fold. As a complementary tool to the full 3D FSI model, this reduced-order model was for fast model simulations and estimation of unknown model parameters. The results were shown to be promising. However, before this tool can be used more extensively, its limitation should be carefully studied. Specifically, it would be useful to know when such a model has good performance and when it does not; and if it does not, what might be done to improve its performance.

Previously, there has been limited study on the reduced-order FSI models and their comparison with full 3D models. In [45], one such comparison was done, but the study was limited to mostly 2D stationary vocal folds, and so there was no comparison of the vocal fold vibration. In Zhang et al. [76], the authors used an experimental setup to study the effects of several parameters such as vocal fold layer stiffness and medial surface thickness on the vibration and compared the results with theoretical prediction that was based on the Bernoulli principle for the flow. However, the comparison was qualitative and there was no detailed discussion on the vibration pattern.

As a reduced-order model may be very useful in the development and applications of high-fidelity models, in this work, we aim to study its performance in a relatively broader parameter space. In particular, we will use an idealized 3D vocal fold model and full 3D FSI

simulations to assess accuracy of the hybrid, reduced-order model based on the Bernoulli principle for the flow and 3D solid mechanics. We will systematically vary the medial surface thickness, assumption for the tissue material behavior, and subglottal pressure for this investigation.

5.2   Setup of FSI models

An illustration of the vocal fold and flow domain could be found in Figure 5.1. A rectangular domain is used to represent the trachea with its walls assumed to be rigid. A pair of vocal folds is placed symmetrically in the domain with length $L = 2$ cm, width $W = 1.3$ cm, and depth $D = 1$ cm. Two different values are adopted for the medial surface thickness, T, a larger one with $T=0.35$ cm and a smaller one with $T=0.175$ cm. The vocal fold is meshed in the commercial software COMSOL Multiphysics (version 4.3) with approximately 18,000 hexahedral elements and 80,000 vertex nodes. For the boundary conditions, the left and right, anterior and posterior surfaces of the vocal fold, i.e., all the sides attached to the rectangular box, are treated as fixed surfaces, while the other surfaces in contact with airflow are free to move. The vocal fold is initially placed to have a small gap of 0.02 cm to enable the flow-induced vibration. The airflow is driven from left (inlet) to right (outlet) by a constant pressure drop between the subglottal pressure P_{sub} at the inlet and reference supraglottal pressure $P_{out} = 0$ kPa at the outlet. The total length of the rectangular box is 12 cm and the vocal fold starts from 2 cm from the inlet. The flow is assumed to be incompressible and is governed by the viscous Navier-Stokes equation in the full 3D model.
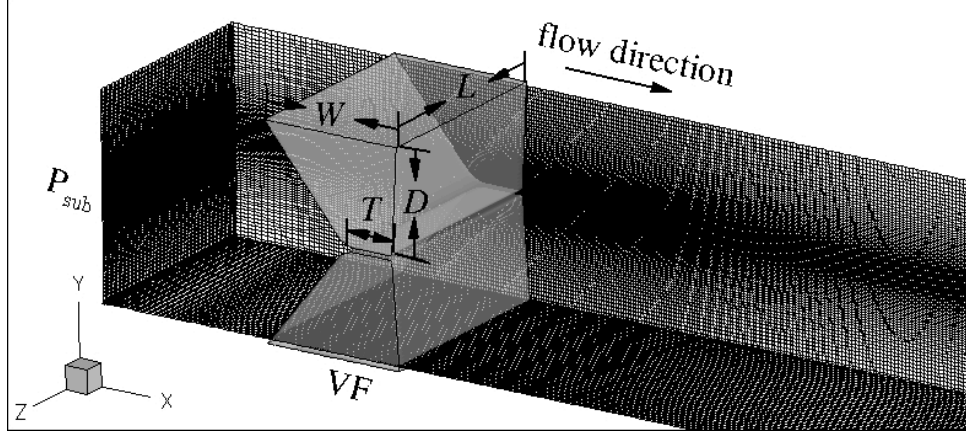
Figure 5.1. Illustration of the idealized vocal fold model and the computational domain used in this study.

Despite the anisotropic effect and layered structures found in the real vocal fold tissue, the vocal fold used in this work is assumed to be isotropic and homogenous. Two tissue material assumptions, i.e., the Saint-Venant model as discussed in Chapter 2 and a hyperelastic, two-parameter Mooney-Rivlin model are incorporated. The Mooney-Rivlin model is one of popular models for representing large deformations of soft tissues [80,81]. The strain energy density function for this model is given as

$$W = \alpha_{10}(\bar{I}_1 - 3) + \alpha_{01}(\bar{I}_2 - 3) + K/2(J-1)^2 \tag{6}$$

where K represents bulk modulus, α_{10} and α_{01} are empirically determined material constants, and $J = \det(F)$ with F standing for the deformation gradient. In addition, $\bar{I}_1$ and $\bar{I}_2$ are given by

$$\begin{aligned} \bar{I}_1 &= J^{-2/3} I_1; & I_1 &= \lambda_1^2 + \lambda_2^2 + \lambda_3^2 \\ \bar{I}_2 &= J^{-4/3} I_2; & I_2 &= \lambda_1^2 \lambda_2^2 + \lambda_2^2 \lambda_3^2 + \lambda_3^2 \lambda_1^2 \end{aligned} \tag{7}$$

where I_1, I_2 are the first and the second invariants of the unimodular component of the left Cauchy–Green deformation tensor, and λ_1, λ_2, λ_3 are the principle stretches of the deformation gradient. As a result, the constitutive relationship for the Mooney-Rivlin model is described as

$$\sigma_{ij}^K = \beta_0 \delta_{ij} + \beta_1 C_{ij} + \beta_2 [C_{ij}]^{-1} + K(J-1)J[C_{ij}]^{-1} \tag{8}$$

where σ_{ij}^K is the second Piola-Kirchhoff stress tensor, C_{ij} is Cauchy-Green deformation tensor and the coefficients are given by

$$\beta_0 = 2\alpha_{10}\frac{1}{J^{2/3}} + 2\alpha_{01}\frac{I_1}{J^{4/3}}, \qquad \beta_1 = -2\alpha_{01}\frac{1}{J^{4/3}}, \qquad \beta_2 = -2\alpha_{10}\frac{I_1}{3J^{2/3}} - 2\alpha_{01}\frac{I_2}{3J^{4/3}} \tag{9}$$

More detailed description about the Mooney-Rivlin model could be found in [80,81] and Tian et al. [82].

In both tissue models, the material density is 1.04 kg/m^3 [23], Poisson's ratio is 0.475, and mass damping is 0.05 s^{-1}. In the Saint-Venant model, Young's modulus is set to be $E = 15$ kPa. When comparing to the Mooney-Rivlin model, it has been shown that these two models could be related to each other, under small-strain conditions, by the following relationships between the material constants

$$2(\alpha_{10} + \alpha_{01}) = G, \qquad \nu = (3K - 2G)/(6K + 2G) \tag{10}$$

where G is the shear modulus and ν is Poisson's ratio in the Saint-Venant model. In the current case, $\alpha_{10} = 2.29$ kPa and $\alpha_{01} = 0.25$ kPa are used in the Mooney-Rivlin model to match the specified stiffness of the Saint-Venant model. The solid dynamics is solved through an explicit method with time step size $\Delta t = 0.0025$ ms, which leads to about 4000 steps for each vibration cycle that is approximately at 100 Hz. The four models are summarized in Table 5.1.

Table 5.1 Four vocal fold models with two medial thicknesses and material descriptions

	T (cm)	Material constants	Material behavior
Model I	0.35	$\alpha_{10} = 2.29$, $\alpha_{01} = 0.25$	Mooney-Rivlin
Model II	0.35	$E = 15$ kPa	Saint-Venant
Model III	0.175	$\alpha_{10} = 2.29$, $\alpha_{01} = 0.25$	Mooney-Rivlin
Model IV	0.175	$E = 15$ kPa	Saint-Venant

5.2.1 The reduced-order FSI model

As discussed in Chapter 4, the reduced-order model consists of a simplified flow model based on the Bernoulli equation and a 3D finite-element tissue model. To apply the Bernoulli equation in the current study, we assume that there is a straight streamline located at the center of the domain and running from the inlet through the glottis. At the inlet, the pressure is assumed to be $p=P_{sub}$, and at the separation point, the pressure is assumed to be $p=P_{out}$. The separation point is the point where the flow starts to separate from the vocal fold surface and the pressure does not vary significantly in the streamwise direction. In this study, the flow separation point is set to be always at the minimum cross section area calculated from the 3D deformed vocal fold. To apply the pressure obtained from the 1D flow model to the surface of the 3D vocal fold, we assume that the pressure at a point on the vocal fold surface, (x_0, y_0, z_0), is equal to the pressure on the streamline at x_0. That is, the pressure within a cross section plane is constant.

5.2.2 The full 3D FSI model

The 3D incompressible flow is governed by Eq. (1) with fluid density 1.13 kg/m^3 for moist air and viscosity at 5×10^{-5} Pa·s (the air viscosity has been increased to the reduce the demand on computational cost). No-slip and no-penetration wall conditions are specified for all flow domain boundaries except the inlet and outlet, where either the inlet or outlet pressure is applied and the velocity is assumed to have a zero normal derivative. An immersed-boundary method is adopted for the flow simulation [27], and the FSI coupling method is described in Tian et al [82]. A non-uniform Cartesian grid with 320×98×72 points is used to discretize the rectangular box illustrated in Figure 5.1. The airflow is driven by a constant pressure difference between the inlet and outlet. The subglottal pressure is set to be $P_{sub}=$ 0.75, 1.0 or 1.25 kPa, which is within the range of the onset pressure for normal human phonation.

5.3   Results

5.3.1   Grid convergence study

A grid convergence study is done for Models I and III with P_{sub} = 1.0 kPa. The non-uniform Cartesian grid is doubled in the region around the vocal fold and also in the flow region immediately downstream the vocal fold. To compare with the baseline simulation, we collect the vibration frequency, displacement magnitude, and phase delay of two points on the medial surface.

The time history of the transverse displacement from Model I is illustrated in Figure 5.2 for a point on the medial surface at the glottal exit.
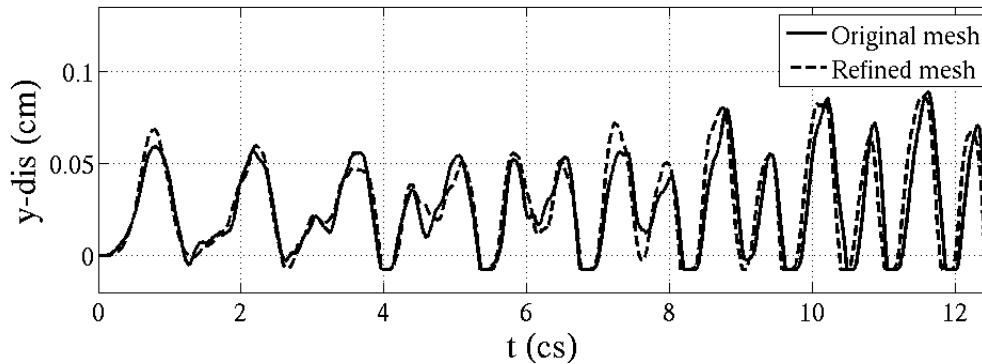
Figure 5.2. The transverse displacement obtained from the two meshes based on Model I under

$$P_{sub} = 1.0 \text{ kPa.}$$

The comparisons on vibration frequency, amplitude and inferior-superior phase delay are listed in Table 5.2. The vibration amplitude is measured as the greatest displacement of one side of the vocal fold in transverse direction. The inferior-superior phase delay is calculated using the

waveform obtained from two tracing points located near the inferior or superior regions, respectively, on the medial surface.

Table 5.2 Vibration frequency f, amplitude d, and phase delay ϕ obtained from the baseline and refined meshes

	f (Hz)	d (cm)	ϕ (°)
Original mesh	138	0.067	51
Refined mesh	141	0.070	49
Relative difference	2.0%	4.5%	3.9%

The table shows that the refined mesh simulation and the baseline simulation consistently provide a less than 5% difference on those three fundamental vibration characteristics. For Model III, the comparisons of the two meshes are similar. Therefore, the baseline mesh is considered to be acceptable for further investigations in this work.

5.3.2 Vibration pattern

Data collection is done for around ten vibration cycles after sustained vibration of vocal fold is obtained. The vibration characteristics are averaged over these cycles. Since the flow-induced vocal fold vibration is closely related to the eigenmodes of the vocal fold, we first compute the eigenmodes before performing the FSI simulations. The 3D vocal fold used in this chapter has a similar cross section as the 2D vocal fold used in Chapter 2. Therefore, their first eigenmode patterns are similar to each other as well. In the current study, for the vocal fold with larger T, the first eigenmode is a forward-backward motion in streamwise direction with a fundamental frequency of 70 Hz; the second mode is an open-close motion in transverse direction with a frequency of 122 Hz. For the vocal fold with smaller T, the motions from both

67

the first and the second eigenmodes are consistent with those of the vocal fold with larger T and have fundamental frequencies of 73 Hz and 126 Hz respectively.

In the FSI simulations, the vocal fold usually starts to vibrate first with a streamwise-deformation mode and then undergo transitions to a sustained, transverse-deformation vibration. Exceptions to this are Model III or Model IV with the reduced-order FSI simulation. In those cases, the vocal fold is found to be consistently vibrating in the forward-backward mode without mode transition. The mode transition captured in all other cases was also reported in Luo et al [27] using 2D vocal fold simulations.

To further clarify the different established vibration modes, one typical vibration cycle under P_{sub} = 1.0 kPa is shown in Figure 5.3 for each of the following four cases: (1) Model I with full 3D FSI, (2) Model I with reduced-order FSI, (3) Model III with full 3D FSI, and (4) Model III with the reduced-order FSI. In the figure, the dark grey represents the original shape of the vocal fold, while the white region represents the deformed shape.

(a)   (b)   (c)

(d)   (e)   (f)

A).

B).

C).

D).
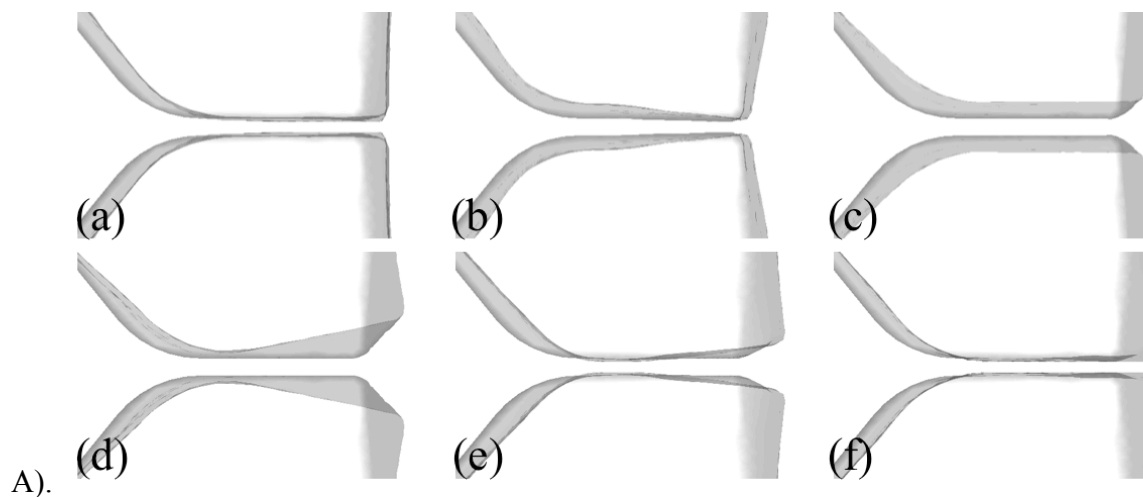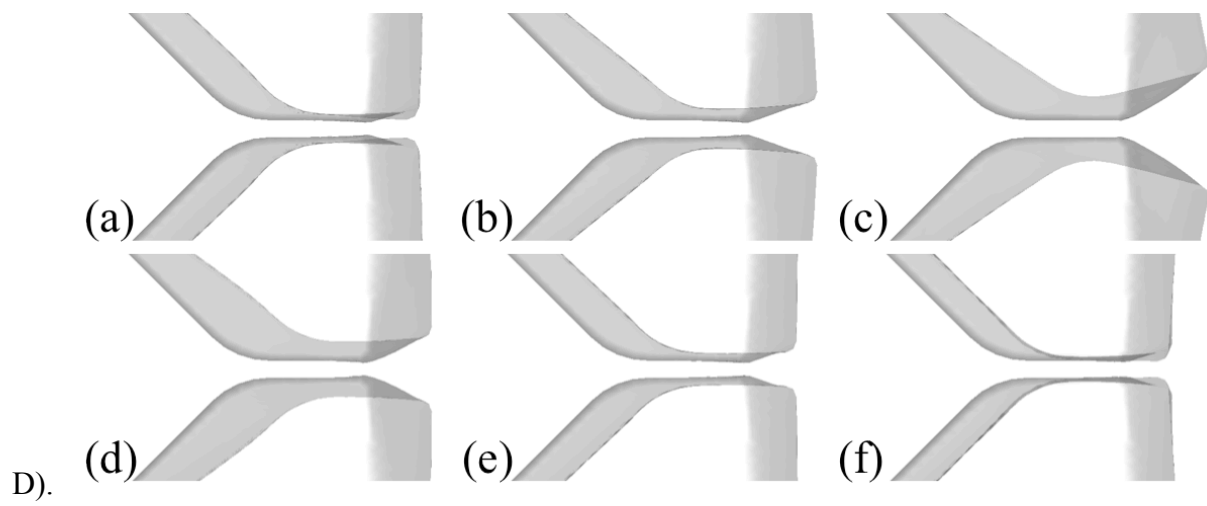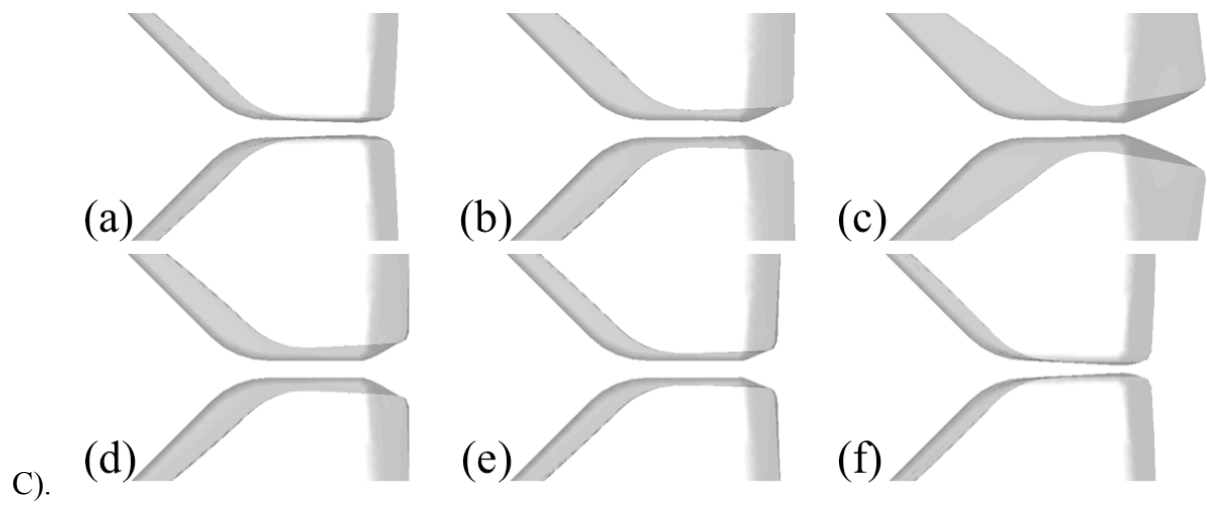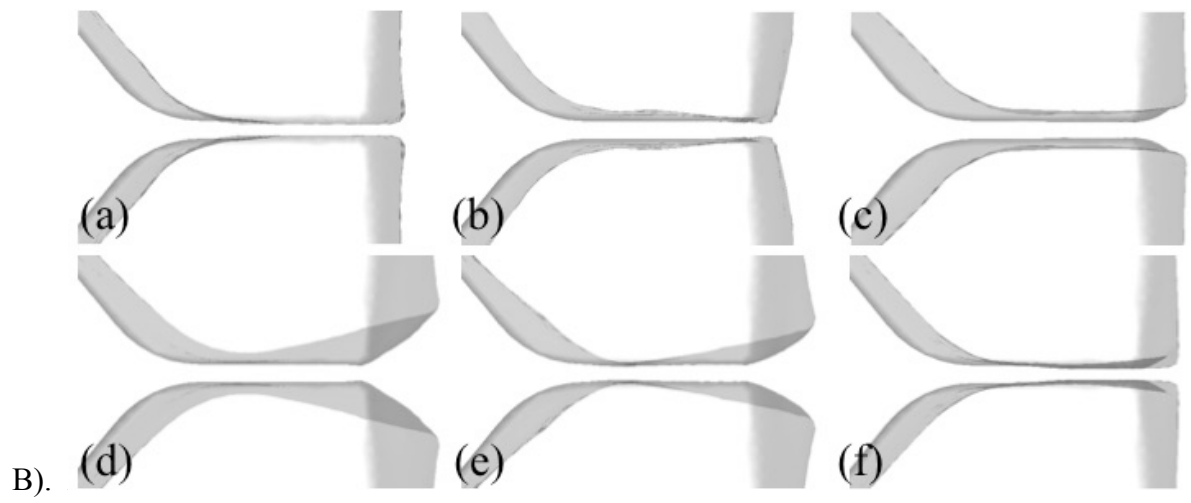
Figure 5.3. Illustration of one typical vibration cycle obtained from two pairs of cases: Model I with full 3D FSI (A) and reduced-order FSI (B); Model III with the full 3D FSI (C) and reduced-order FSI (D); all under P_{sub} = 1.0 kPa. In each case, (a-c) are the opening phase and (d-f) are the closing phase of the vocal fold.

For Model I, the reduce-order FSI model provides a consistent vibration pattern as compared with the full 3D FSI model, which is illustrated in Figure 5.3(A,B). It is apparent that the vocal fold motions are mostly in the transverse direction, which corresponds to the second eignenmode. The vocal fold collision takes place from the inferior region to the superior region along the medial surface and along the longitudinal has the greatest amplitude in the mid-portion. Moreover, the inferior vocal fold starts to open first and forms a divergent glottal shape in Figure 5.3 from (a) to (c) during the opening phase. On the other hand, from (d) to (f) the inferior vocal fold closes first and is followed by the superior vocal fold, generating a divergent glottal shape. Such divergent-convergent glottal shape is closely related to the mucosal wave propagation along the medial surface and commonly discussed in previous studies [1]. Without showing in figures, it should be pointed out that Model II has similar consistent comparison between the full 3D and the reduced-order models.

The vibration pattern between the two FSI models is significantly different when Model III and Model IV are considered. As shown in Figure 5.3(C), when the full 3D FSI model is used, Model III predicts a transverse vibration mode with a high frequency of 130 Hz. However, when the reduced-order FSI model is used, the mode transition cannot be found for Model III. Instead, as shown in Figure 5.3(D), the vocal fold moves mainly in the streamwise direction with

70

a relative low frequency of approximately 70 Hz. The comparison of Model IV is similar to that of Model III.

Unlike Model I and Model II, where the converging-diverging shape is more evident and vocal fold impact takes place over the entire medial surface, in Model III and Model IV the glottis is either straight or convergent, and the impact is more likely to appear near the superior region. This result is thus consistent with [39], which reported that a large medial thickness of vocal fold would promote mucosal wave formation.

5.3.3 Vibration frequency, amplitude and phase delay

To further quantify the predictions of the reduced-order FSI model and the full 3D FSI model, we provide the basic phonation characteristics, e.g., vibration frequency, amplitude, inferior-superior phase delay, and flow rate for comparison. As discussed in [83], vocal fold inferior-superior phase delay has been found important in creating a convergent-divergent glottal configuration. The averaged values for these characteristics under different subglottal pressure are listed in the Table 5.3. We point out that for Model IV with the reduced-order FSI model and $P_{sub} = 1.25$ kPa, the vocal fold deformation becomes too large for the simulation to convergence; therefore, no data were collected for this case.

Table 5.3 Vibration frequency f (Hz), amplitude d (cm), phase delay ϕ (°), and flow rate Q (ml/s) obtained from both the reduced-order model and the full 3D model

		P_{sub} (kPa)	Model I	Model II	Model III	Model IV
f (Hz)	The reduced-order FSI model	0.75	136.3	129.7	75.4	72.7
		1.00	136.8	128.2	77.9	71.8
		1.25	137.7	126.5	76.8	/
	The full 3D FSI model	0.75	138.1	132.7	131.6	128.7
		1.00	138.7	132.7	134.4	126.4

		1.25	139.4	130.0	136.2	/
d (cm)	The reduced-order FSI model	0.75	0.0846	0.0830	0.0697	0.0789
		1.00	0.1198	0.1083	0.0920	0.0928
		1.25	0.1392	0.1373	0.1240	/
	The full 3D FSI model	0.75	0.0837	0.0780	0.0462	0.0680
		1.00	0.1116	0.0950	0.0705	0.1126
		1.25	0.1188	0.1014	0.0962	/
ϕ (°)	The reduced-order FSI model	0.75	37.54	28.71	-9.95	-3.92
		1.00	50.72	32.77	-9.05	0.86
		1.25	59.64	43.68	1.10	/
	The full 3D FSI model	0.75	53.50	41.50	-7.82	4.47
		1.00	57.76	36.52	-9.27	-5.12
		1.25	66.30	44.20	-13.48	/
Q_{max} (ml/s)	The reduced-order FSI model	0.75	554	624	602	648
		1.00	804	980	830	866
		1.25	958	1306	1080	/
	The full 3D FSI model	0.75	488	584	457	584
		1.00	705	886	664	934
		1.25	931	995	916	/

In Table 5.3, the frequencies of sustained vibration in most cases are within the normal human phonation range, i.e., 80~220 Hz [84]; however, exceptions are found for Model III and Model IV with the reduced-order FSI model. In these cases, the sustained vibration frequencies are slightly lower than 80 Hz. The ratio of the vibration amplitude to the vocal fold length is around 10%, which is also reasonable for normal human phonation. For straightforward comparison, the data in Table 5.3 are organized and plotted in Figure 5.4.
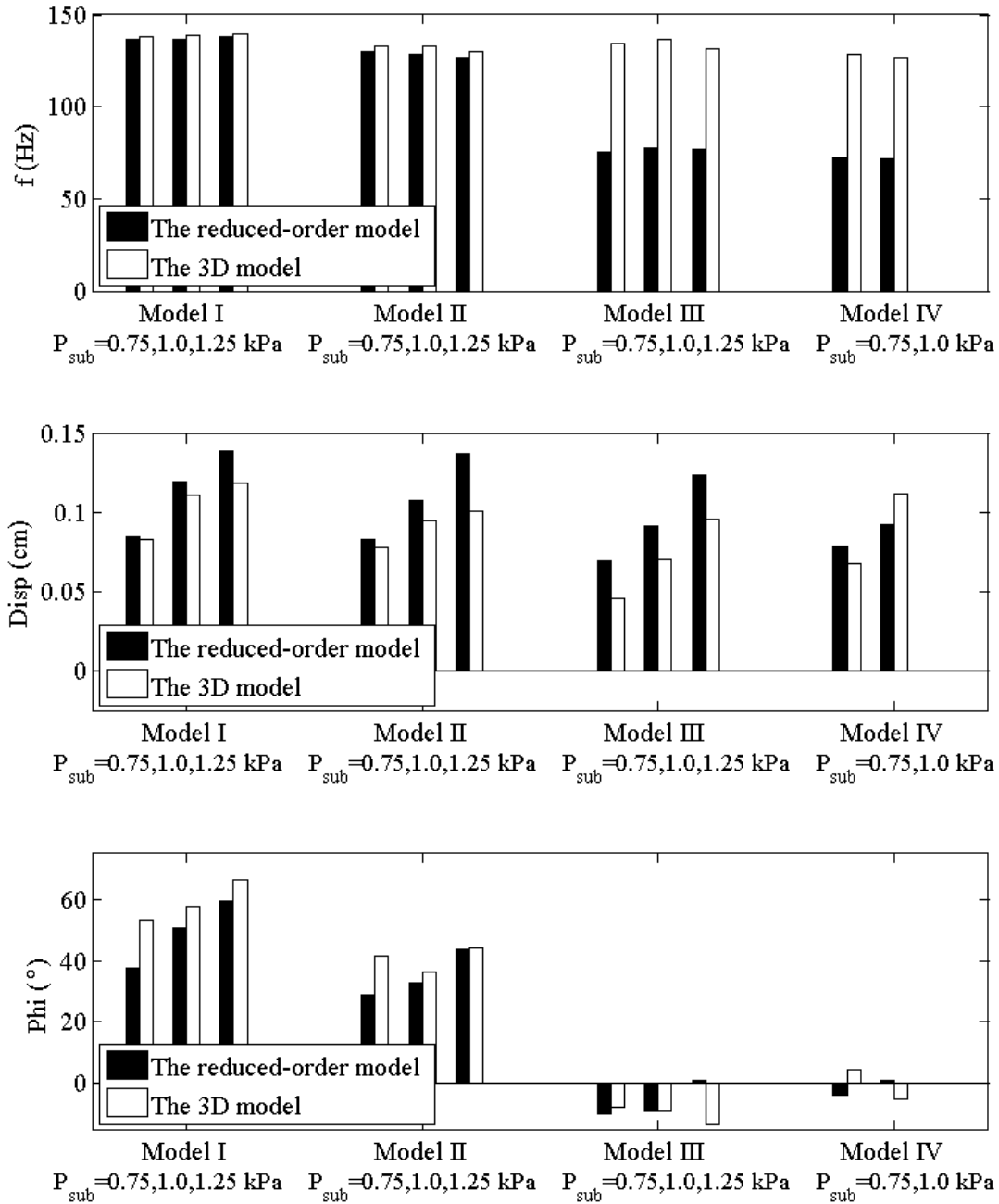
Figure 5.4 Vibration frequency f (Hz), amplitude d (cm), phase delay ϕ (°), and flow rate Q

(ml/s) obtained from the reduced-order model and the full 3D model

From Figure 5.4(a), it is clear that given the specific model, the prediction of the vibration frequency between the two FSI models is generally consistent when the subglottal

pressure is varied. That is, for Model I and Model II, vibration frequency of the reduced-order FSI model is very close to that of the full 3D FSI model for different values of the subglottal pressure; however, for Model III and Model IV, the reduced-order model always predicts a significant lower frequency (40% lower) than the full 3D model. As discussed earlier, such frequency disparity is associated to different vibration patterns predicted by the two FSI models for Model III and Model IV.

Figure 5.4(b) shows that the reduced-order FSI model generally predicts a greater vibration amplitude than the full 3D FSI model in most cases. The only exception is Model IV with P_{sub} = 1.0 kPa, where the full 3D FSI predicts a greater amplitude.

Figure 5.4(c) shows that the reduce-order FSI model generally under-estimates the inferior-superior phase difference as the subglottal pressure is varied. This result is true mostly for Model I and Model II. For Model III and Model IV, the phase difference is small due to the thin thickness of the vocal fold, and the comparison between the two FSI models does not provide particularly meaningful results.

The errors, or relative differences, of vibration characteristics between the reduced-order model and the full 3D model are also calculated, and the results are shown in Table 5.4 for all cases. For each specific case, the full 3D FSI result is assumed to be the reference based on which the relative differences are calculated. A plus sign means a relative increase in the prediction of the reduced-order FSI model, and a minus sign means a decrease.

Table 5.4 Errors in the vibration frequency, largest amplitude, phase delay, and flow rate

obtained from the reduced-order model and the full 3D model

	P_{sub} (kPa)	Model I	Model II	Model III	Model IV
f	0.75	+1.3%	+2.3%	+43.0%	+41.1%
	1.00	+1.4%	+3.4%	+42.0%	+42.3%
	1.25	+1.2%	+3.1%	+42.3%	/
d	0.75	-1.1%	-6.4%	-50.9%	-16.0%
	1.00	-7.3%	-14.0%	-30.5%	+17.6%
	1.25	-17.2%	-35.4%	-28.9%	/
ϕ	0.75	+29.8%	+30.8%	-27.2%	+187%
	1.00	+12.2%	+10.3%	+2.4%	+116%
	1.25	+10.0%	+1.2%	+108%	/
Q_{max}	0.75	-13.5%	-6.8%	-31.7%	-11.0%
	1.00	-14.0%	-10.6%	-25.0%	-7.3%
	1.25	-2.9%	-31.3%	-17.9%	/

From this table, the error in vibration frequency of the reduced-order FSI is within 5% for Model I and Model II, where the vocal fold thickness is large. However, in case of small vocal fold thickness as in Model III and Model IV, the error of the reduced-order FSI is approximately 40%. This result shows the vocal fold thickness can greatly affect accuracy of the reduced-order model in terms of vibration frequency. A similar conclusion could be drawn in terms of vibration amplitude. For Model I and and Model II with large vocal fold thickness, the error in the amplitude by the reduced-order model is reasonable, albeit it is increasing as P_{sub} is raised. However, for Model III and Model IV with small vocal fold thickness, the error in the amplitude can reach as much as 50%.

In these comparisons, the assumptions of the tissue behavior in general do not make significant difference. This result can be seen from Table 5.4, where the error of the reduced-order FSI for Model I is similar to that for Model II, and the error for Model III is similar to that for Model IV. However, exceptions can also be found in some cases, e.g., between Model I and Model II when P_{sub}=1.25 kPa.

5.3.4 Waveforms of gap width and air velocity

To study the temporal waveform of the glottal gap width, one point near the superior region of the medial surface is used, and its time-dependent transverse displacement is normalized by its greatest displacement over time. Comparison between the full 3D FSI and the reduced-order FSI is given in Figure 5.5. The waveforms are also shifted in time for easy comparison.
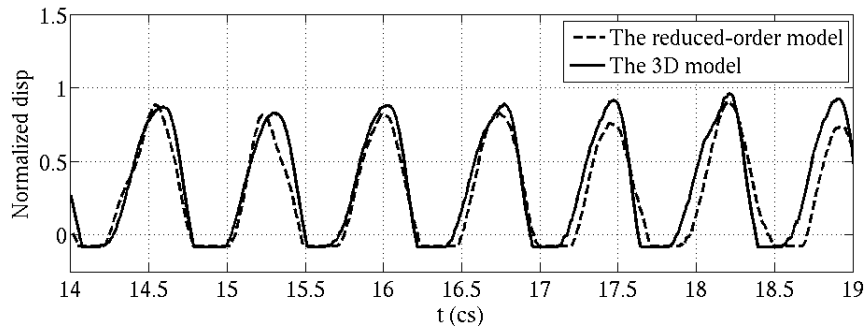
(a).
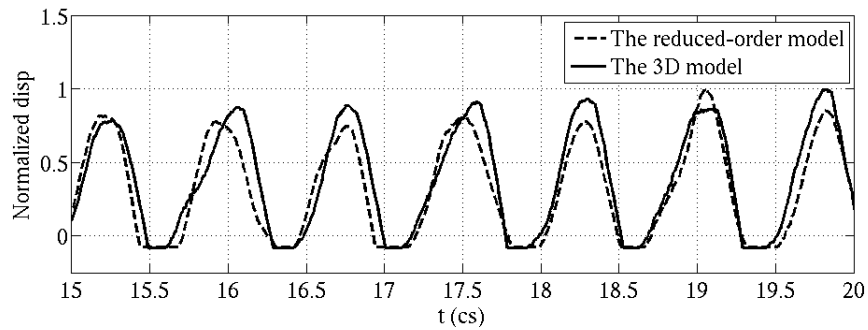
(b).
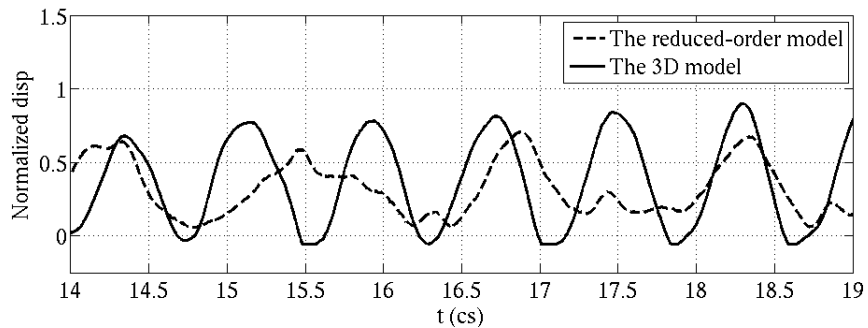
(c).

Figure 5.5 Comparison between the reduced-order FSI model and the full 3D FSI model in terms

of the normalized gap width for (a) Model I, (b) Model II, and (c) Model IV with P_{sub} = 1.0 kPa

From Figure 5.5 (a) and (b), it is seen that the waveform of gap width predicted by the

reduced-order FSI is generally close to that by the full 3D FSI simulation for Model I and Model

II, even though the collision time in the reduced-order FSI simulation is slightly longer than that

in the full 3D FSI simulation. Another difference is that the reduced-order FSI model provides

slightly lower estimates of the open quotient and the skewing quotient. When it comes to Model

IV, the waveform of gap width is very different between the reduced-order FSI simulation and

the full 3D FSI simulation, due to the significantly different vibration modes predicted by the

two simulations. Note that the result from Model III is similar to that from Model IV and thus is

not further discussed here.

The temporal waveform of the flow velocity in the glottis as measured on the centerline

in the glottis is extracted and shown in Figure 5.6. Again, the waveform is shifted in time for

easy comparison. In these comparisons, it is seen that the reduced-order FSI model leads to a

much wider flow phase than the full 3D FSI model, but its peak velocity is lower than that of the

full 3D model. This result can be understood since in the reduced-order model, the viscous effect

on the flow was ignored (so the flow has longer duration) and the flow speed is averaged across

the glottal gap (so its amplitude is lower). It should be pointed out that the waveforms of the two

simulations are substantially different for Model III and IV due to different vibration pattern and

glottal configuration.
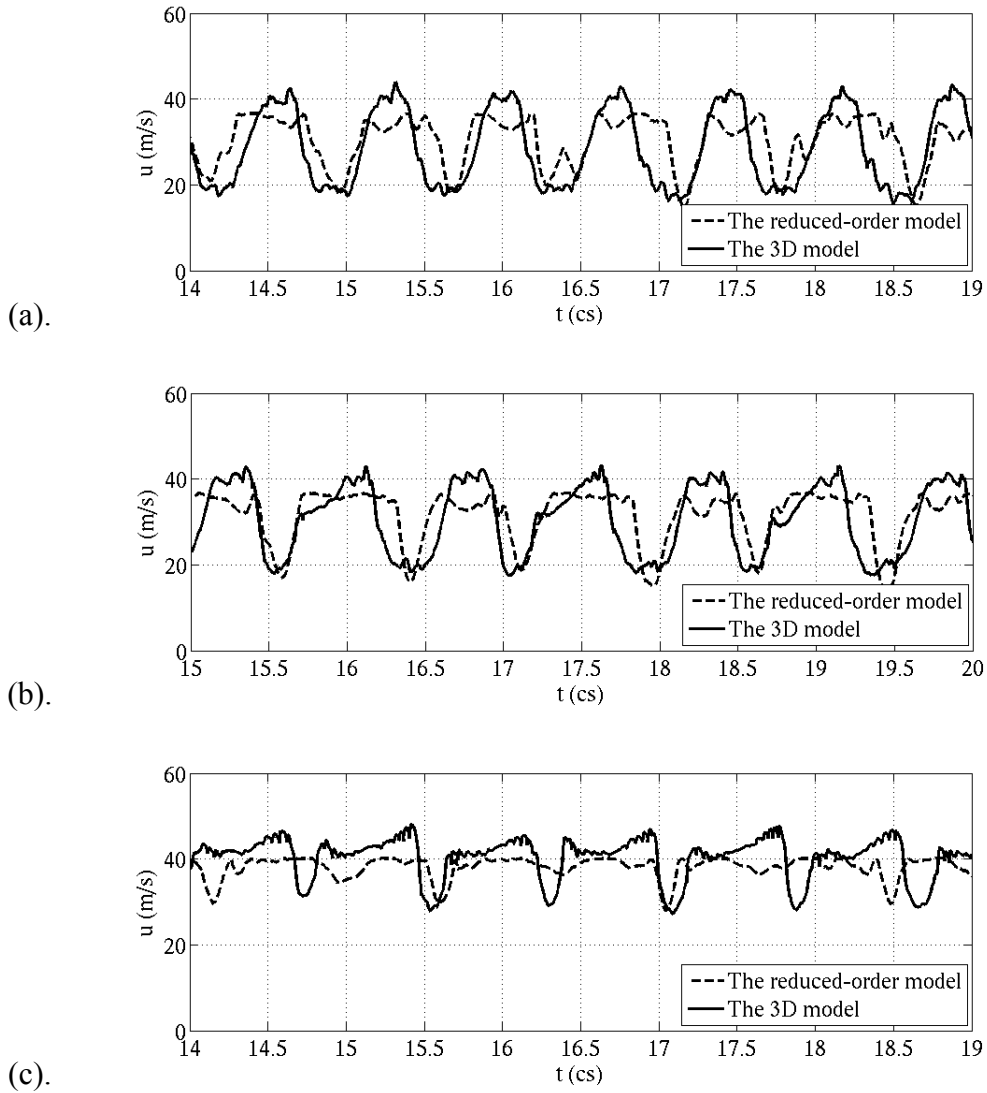
Figure 5.6 Comparison of the temporal waveform of the velocity in the glottis between the
reduced-order FSI model and the full 3D FSI model; (a) Model I, (b) Model II, and (c) Model IV

with $P_{sub} = 1.0$ kPa

5.3.5 Pressure distribution

As described previously, the flow model in the reduced-order FSI simulation is based on

the Bernoulli principle, which governs the pressure and velocity variations in the glottis prior to

the flow separation point. Therefore, accuracy of the pressure distribution on the vocal fold surface is a key factor to examine to understand the results completely. Take Model I under P_{sub} = 1.0 kPa for example. The pressure distribution along the centerline of the domain is extracted at different time snapshots and is shown in Figure 5.7 for the close phase, convergent phase, open phase, and divergent phase. Along with the pressure distribution, the area of the cross section, A, is also plotted to give a sense of the glottal configuration at the moment.

Figure 5.7 Comparison of the pressure distribution along the centerline between the reduced-order FSI model and the full 3D FSI model for Model I with P_{sub} = 1.0 kPa. (a) Close phase, (b) convergent phase, (c) open phase, and (d) divergent phase. In each case, corresponding cross section area, A, is also plotted.

From Figure 5.7, it is shown that the reduced-order FSI model is able to predict the pressure distribution in the glottis well when the glottal configuration is divergent, convergent, or near the maximum opening phase. The reduced-order FSI model results in a steeper pressure slope when the vocal fold moves to the fully closed phase and the glottal gap width becomes small. Such difference is likely caused by the viscous effect in the full 3D FSI model. Another observation is that in the reduced-order FSI simulation, the location of the minimum pressure is always closer to the inferior region as compared to the full 3D simulation. This result suggests that to further improve the accuracy of the reduced-order model, the location of the separation point may need to be moved downstream.

To investigate how the vocal fold thickness plays a role in predicting the pressure distribution for these two FSI models, we use the case Model III with P_{sub} = 1.0 kPa for illustration. From Figure 5.8, it is shown that the reduced-order FSI model is able to capture overall pressure distribution in the glottis for all glottal configurations. However, considerable differences can be observed between the reduced-order FSI model and the full 3D model. More specifically, the pressure drop in the glottis of the reduced-order model is much greater than that of the full 3D FSI model. As in Model I, the location of the minimum pressure from the reduced-order FSI model is closer to the inferior region as compared with the full 3D model, which suggests that this point should be moved further downstream to improve the model accuracy.
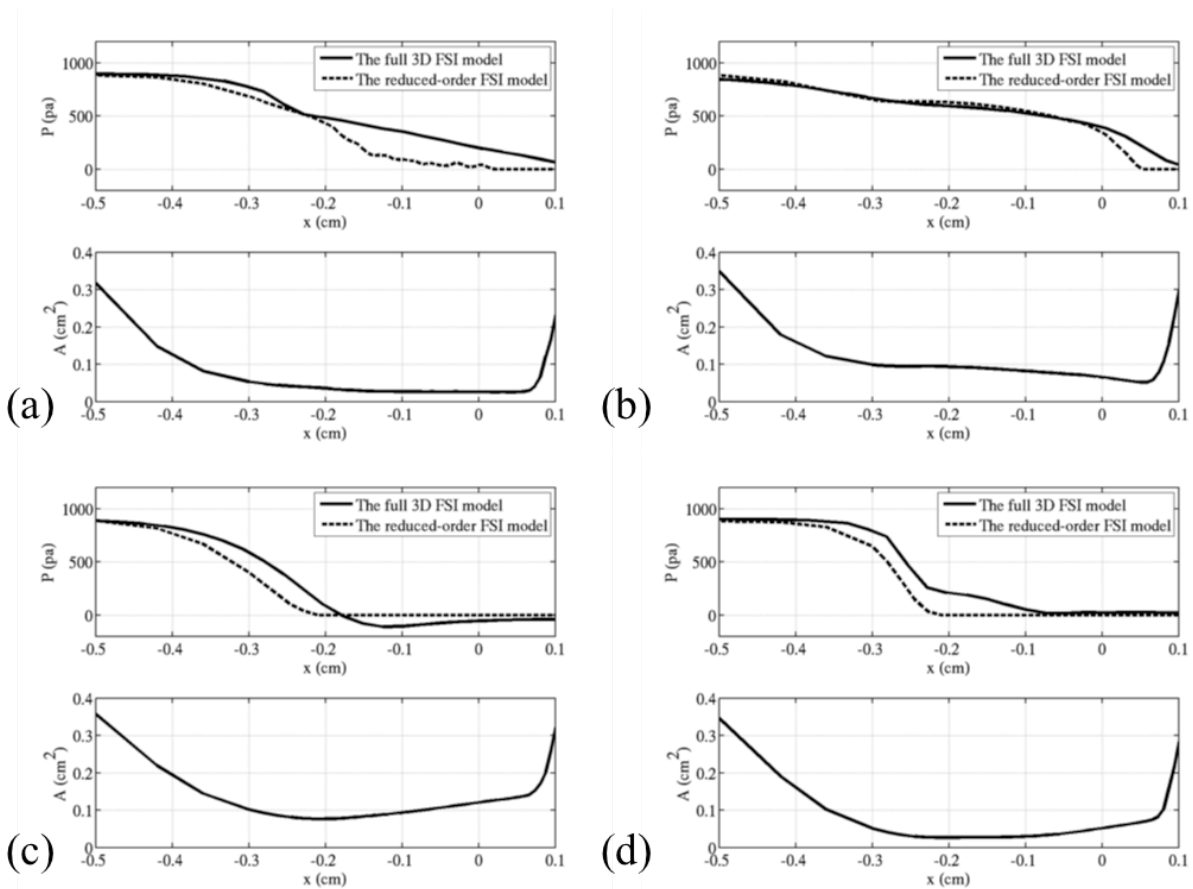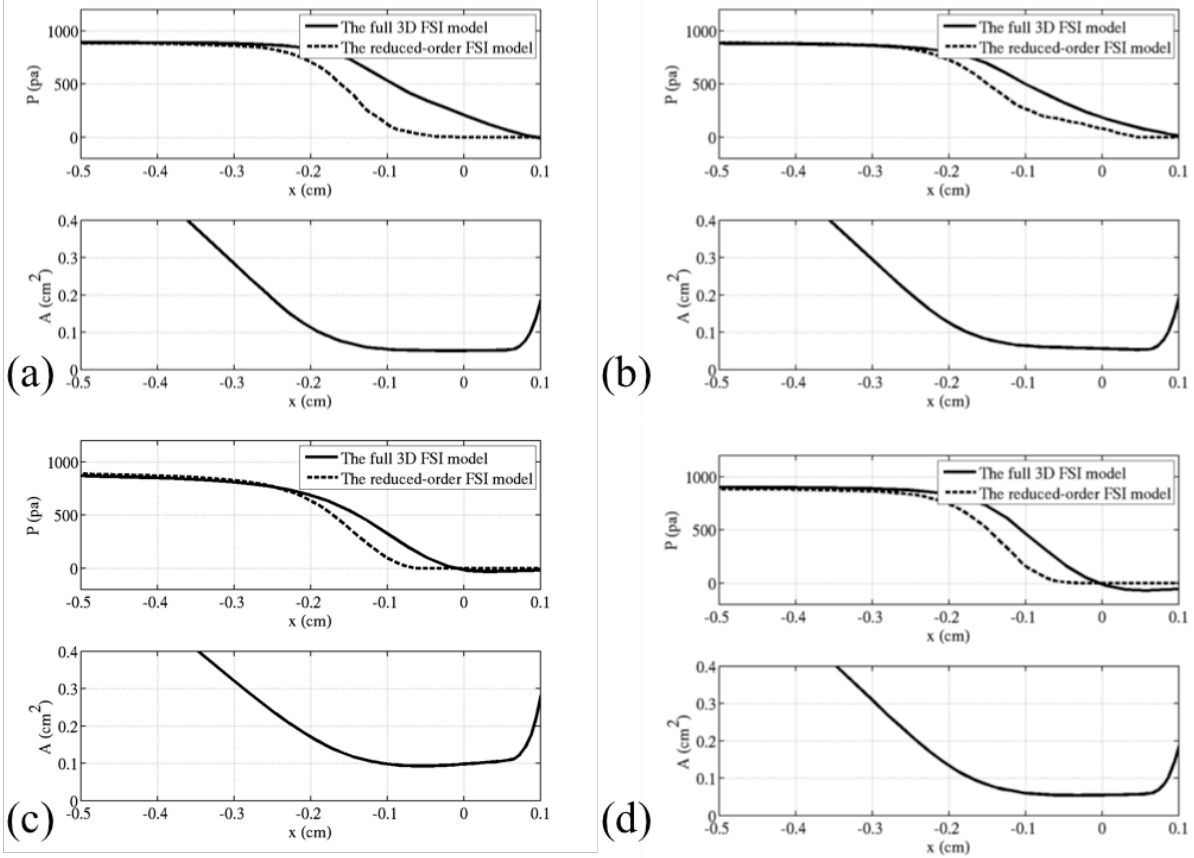
Figure 5.8 Comparison of the pressure distribution along the centerline between the reduced-order FSI model and the full 3D FSI model for Model III with P_{sub} = 1.0 kPa. (a) Close phase, (b) convergent phase, (c) open phase, and (d) divergent phase. In each case, corresponding cross section area, A, is also plotted.

5.4   Conclusions

In this chapter, we have designed an idealized vocal fold to compare predictions of two FSI models, i.e., a reduced-order FSI model with drastically simplified flow representation, and a full 3D FSI model incorporating 3D viscous unsteady flow. In both models, the vocal fold is represented by a 3D nonlinear finite-element model. The objective is to investigate the accuracy of the reduced-order FSI model as compared with the full 3D model. The medial thickness, the

81

material behavior or the constitutive law of the tissue, and the subglottal pressure are varied systematically during the study.

For both the reduced-order FSI model and the full 3D FSI model, sustained vocal fold vibration is achieved. The results show that the medial thickness has the greatest influence on the performance of the reduced-order FSI model. Specifically, when the medial thickness is large, the results from the reduced-order FSI model are consistent with those from the full 3D FSI model, including the vibration frequency, amplitude, deformation pattern, and mucosal wave along the vocal fold surface. However, when the medial thickness is small, the reduced-order FSI model may lead to a different vibration mode and frequency than that from the full 3D FSI model.

As compared with the medial thickness, other model assumptions such as the subglottal pressure and the tissue behavior have relatively less influence on the accuracy of the reduced-order FSI model. As the subglottal pressure is raised, the vocal fold generally has greater deformation amplitude, which was captured by both the reduced-order FSI and full 3D FSI models. When the Mooney-Rivlin model is used for the tissue behavior, the vocal fold has less deformation as compared with the Saint-Venant model, due to the nonlinear and stiffening effect in the former case.

The pressure distribution in the glottis shows that in the reduced-order FSI model, the pressure has a great drop along the streamline than in the full 3D FSI model. This result suggests that we might need to adjust the location of flow separation in the reduced-order model to make it more accurate. Further study will be needed to investigate this issue.

CHAPTER 6   CONCLUSIONS AND FUTURE STUDY

6.1   Conclusions

In this thesis, we have focused on computational modeling of the fluid-structure interaction (FSI) for vocal fold vibration during phonation. The computational setup includes 2D and 3D FSI models with idealized geometries, as well as anatomical geometries based on medical imaging. These models are developed for two goals in general. In the first goal, we aim to understand fundamental FSI process of phonation and thus would like to single out effects of certain aspect such as the role of the nonlinear tissue mechanics. Understanding of these fundamental effects will provide useful guidance for development of more advanced computational models in the future, e.g., those for clinical applications.

In the second goal, we aim to explore the issues of developing high-fidelity, patient-specific computational models that ultimately could be used in clinic for improved treatment of voice disorders. These issues include the experimental procedure to produce necessary data input for model development, creation and simulation of the FSI models from imaging data, handling of unknown model parameters, and validation of patient-specific characteristics. With these two goals, four specific studies were carried out in this thesis.

In the first study, the effect of geometric nonlinearity in vocal fold modeling is investigated. A 2D computational model with idealized geometry is constructed, in which the vocal fold tissue is assumed to be simply linearly elastic. For comparison, two models, i.e., model I under small strains assumption and model II with large displacement and rotations incorporated, are applied to study the effect of the finite displacement on the vocal fold dynamics and glottal airflow. Results show that vibration amplitude, impact stress, and flow rate obtained

from model I are consistently lower compared with model II under given subglottal pressure. In cases where the subglottal pressure becomes high, e.g., 0.8 kPa in the present study, the vibration mode of the vocal fold predicted by model I is composed of natural modes with lower frequencies than those of model II. In general, the geometric nonlinear effect is amplified during vocal fold collision. In addition, the fluid-structure coupling further enhances the contribution made by geometric nonlinearity to vocal fold vibration. Although the quantitative results are limited to the specific models assumed in the present work, the current study suggests that geometric nonlinearity should be incorporated in a computational model for accurate simulation of the vocal fold dynamics and prediction of the impact stress.

In the second study, a novel *in vivo* methodology is developed using evoked rabbit phonation to investigate the model development issues and meet the future need of a clinically useful tool. In this study, the rabbit's thyroid and cricoid cartilages are successfully sutured *in vivo* to elicit rabbit phonation. Aerodynamic and acoustic measurements are conducted during *in vivo* phonation as well as high-speed imaging. Afterwards, MR imaging is performed on the excised larynx with different scanning protocols. Results show the new approach produces consistent phonation characteristics with previous electrical stimulation. More importantly, the suture method allows the vocal fold tissue to stay in the adducted phonatory position after excision, which retains the vocal fold configuration during MR imaging. Given that the geometric features could significantly affect vocal fold vibration, the new *in vivo* technique would consequently improve quality of the computational models based on the imaging data.

In the third study, an approach towards the development of a high-fidelity computational tool for surgical treatments is described. Experimental studies on evoked rabbit phonation are performed with both *in vivo* measurement and MR scanning for excised larynges. Computational

simulations based on reconstructed realistic laryngeal models from medical images are conducted for parameterized explorations and subject-specific validations. In the numerical approach, a hybrid model composed of simplified 1D flow solver coupled with full 3D tissue mechanics solver is created to estimate the unknown elastic constants of the vocal fold layers. Results show that the laryngeal anatomy with considerable realistic geometric features is successfully reconstructed from MR scans. Based on a two-layer simplification with isotropic tissue assumption, the individual unknown material properties are identified and shown to be within the range of population data. The reconstructed computational model is validated through comparison with individual-specific characteristics of vocal fold vibration that are measured from the *in vivo* phonation experiment, e.g., vibration frequency, amplitude, and waveform of displacement. Generally, the simulated results are able to match those experimental measurements.

In the fourth study, the comparison between the reduced-order FSI model and the full 3D FSI model is investigated using an idealized vocal fold geometry. Effects of the subglottal pressure, material behavior, and medial thickness on the differences between predictions of the two FSI models are discussed in detail. Results show that the reduced-order FSI model can successfully reproduce the results from the full 3D FSI model when the medial thickness is large; however, when the medial thickness is small, the reduced-order FSI model can be significantly different from the full 3D model.

6.2 Future work

This work only represents a preliminary step toward development of high-fidelity, patient-specific computational models that could eventually be used in clinical care of voice

disorders. Substantial work will be needed from several perspectives to further advance the methodology of model creation and validation.

First, the performance of the current reduced-order FSI model using the simple Bernoulli principle is not entirely satisfactory. In particular, significant differences between the reduced-order model and the full 3D model were observed when the medial thickness of the vocal fold is small. In the future, we could try different approaches to estimate the location of the flow separation and study its effect on the model performance. In such a study, the full 3D FSI model can be used as the reference for comparison and also as a tool to calibrate the separation point and to study the detailed flow physics, e.g., how does the flow separation depends on the glottal configuration and flow conditions. We envision such a study could significantly improve accuracy of the reduced-order FSI model and expand its future usage.

Second, some procedures in the process of model creation are manual and thus very time-consuming, for example, segmentation of the vocal fold tissue from the image data and the identification of unknown model parameters. In the future, advanced tools could be incorporated to improve efficiency of model generation. For segmentation, there are automatic and semi-automatic software tools available for general purposes of processing medical images. Those tools could potentially be adapted in the current context to assist with reliable and accurate segmentation. For parameter identification, existing optimization toolboxes and algorithms could be used to automate the search process. This improvement would be very useful when there are more model parameters to identify and when there is a large parameter space to explore.

Third, the current imaging modality requires excision of the larynx. In the future, alternative *in vivo* imaging approaches such as Computed Tomography (CT) will likely have to

be used. Segmentation of the images produced using these approaches, the uncertainties associated with the segmentation process, and their effect on the computational model will need to be investigated. In addition, the experimental procedure may have to be modified correspondingly to accommodate the imaging protocol and to collect the aerodynamic/acoustic measurements required for model input (e.g., flow rate and subglottal pressure) and model validation (e.g., vibration frequency and vocal fold displacement).

Fourth, in order to develop computational models to predict surgical outcome of medialization laryngoplasty, the anatomical and biomechanical effects of the implant that is inserted into the paralyzed vocal fold should be incorporated in the finite-element model of the vocal fold. As a result, the surgically altered vocal fold will have different eigenmodes and will respond the aerodynamic load differently than the normal vocal fold. A fundamental study should be done to investigate the parameterization of the implant and how to incorporate it into a FSI model. Furthermore, combined experimental and computational studies are needed to develop and validate subject-specific computational models that include the 3D anatomy and geometric/material design of the implant.

Finally, development of the computational models for human subjects is the ultimate goal for this line of research. Substantial work still needs to be done regarding human imaging, image processing, model creation, unknown parameters, implant incorporation, and model validation. These tasks will require close collaboration of computational engineers, medical scientists, and surgeons over the next decade or two.

REFERENCES

[1]   Sjoerdsma, R. D., 1996, "Bookshelf: 'Principles of Voice Production,' by Ingo R. Titze,"
        J. Sing. - Off. J. Natl. Assoc. Teach. Sing., **52**(5), p. 41.

[2]   NIDCD, 2007, "National Institute on Deafness and Other Communication Disorders
        (NIDCD)."

[3]   Swanson, E. R., Abdollahian, D., Ohno, T., Ge, P., Zealear, D. L., and Rousseau, B.,
        2009, "Characterization of raised phonation in an evoked rabbit phonation model,"
        Laryngoscope, **119**(7), pp. 1439–1443.

[4]   Yan, Y., Ahmad, K., Kunduk, M., and Bless, D., 2005, "Analysis of vocal-fold vibrations
        from high-speed laryngeal images using a Hilbert transform-based methodology," J.
        Voice, **19**(2), pp. 161–175.

[5]   Anderson, T. D., Spiegel, J. R., and Sataloff, R. T., 2003, "Thyroplasty revisions:
        frequency and predictive factors," J Voice, **17**(3), pp. 442–448.

[6]   Kimura, M., Mau, T., and Chan, R. W., 2010, "Viscoelastic properties of phonosurgical
        biomaterials at phonatory frequencies.," Laryngoscope, **120**(4), pp. 764–8.

[7]   Ford, C. N., Staskowski, P. A., and Bless, D. M., 1995, "Autologous collagen vocal fold
        injection: a preliminary clinical study.," Laryngoscope, **105**(9 Pt 1), pp. 944–948.

[8]   Long, J. L., Neubauer, J., Zhang, Z., Zuk, P., Berke, G. S., and Chhetri, D. K., 2010,
        "Functional testing of a tissue-engineered vocal fold cover replacement.," Otolaryngol.
        Head. Neck Surg., **142**(3), pp. 438–40.

[9]   Titze, I. R., Hitchcock, R. W., Broadhead, K., Webb, K., Li, W., Gray, S. D., and Tresco,
        P. a, 2004, "Design and validation of a bioreactor for engineering vocal fold tissues under
        combined tensile and vibrational stresses.," J. Biomech., **37**(10), pp. 1521–9.

[10]   Bennett, Suzanne, and B. W., 1973, "Acceptability ratings of normal, esophageal, and
        artificial larynx speech," J. Speech, Lang. Hear. Res., **16**(4), pp. 608–615.

[11]   Seikel, J., King, D., and Drumright, D., 2009, Anatomy and physiology for speech,
        language, and hearing.

[12]   Titze, I. R., 1994, Principles of Voice Production, Prentice-Hall, Englewood Cliffs, NJ.

[13]   Zemlin, W., 1997, Speech and Hearing Science: Anatomy & Physiology, Boston, MA.

[14]   Alipour, F., Finnegan, E. M. E., and Jaiswal, S., 2013, "Phonatory characteristics of the
        excised human larynx in comparison to other species," J. Voice, **27**(4), pp. 441–447.

[15]   Jiang, J. J., and Titze, I. R., 1994, "Measurement of vocal fold intraglottal pressure and

impact stress.," J. Voice, **8**(2), pp. 132–44.

[16]   Jiang, J. J., Zhang, Y., and Ford, C. N., 2003, "Nonlinear dynamics of phonations in excised larynx experiments," J. Acoust. Soc. Am., **114**(4), p. 2198.

[17]   Finnegan, Eileen M.; Alipour, F., 2009, "Phonatory Effects of Supraglottic Structures in Excised Canine Larynges," AUTHORS MANUSCRIPT- ist aber auch im J. Voice, **23**(1), pp. 51–61.

[18]   Scherer, R. C., Shinwari, D., De Witt, K. J., Zhang, C., Kucinschi, B. R., and Afjeh, A. A., 2001, "Intraglottal pressure profiles for a symmetric and oblique glottis with a divergence angle of 10 degrees," J. Acoust. Soc. Am., **109**(4), pp. 1616–1630.

[19]   Mendelsohn, A., and Zhang, Z., 2010, "Phonation threshold pressure and frequency in a two-layer physical model of the vocal folds: Comparison between experiment and theory.," J. Acoust. Soc. Am., **128**(4), p. 2474.

[20]   Drechsel, J. S., and Thomson, S. L., 2008, "Influence of supraglottal structures on the glottal jet exiting a two-layer synthetic, self-oscillating vocal fold model.," J. Acoust. Soc. Am., **123**(6), pp. 4434–45.

[21]   Ishizaka, K., and Flanagan, J. L., 1972, "Synthesis of voiced sounds from a two-mass model of the vocal cords," Bell Syst. Tech. J., **51**(6), pp. 1233–1268.

[22]   Jiang, J., and Zhang, Y., 2002, "Chaotic vibration induced by turbulent noise in a two-mass model of vocal folds," J. Acoust. Soc. Am., **112**(5 Pt 1), pp. 2127–2133.

[23]   Alipour, F., Berry, D. a, and Titze, I. R., 2000, "A finite-element model of vocal-fold vibration.," J. Acoust. Soc. Am., **108**(6), pp. 3003–3012.

[24]   Gunter, H. E., 2003, "A mechanical model of vocal-fold collision with high spatial and temporal resolution," J. Acoust. Soc. Am., **113**(2), p. 994.

[25]   Hunter, E. J., Titze, I. R., and Alipour, F., 2004, "A three-dimensional model of vocal fold abduction/adduction.," J. Acoust. Soc. Am., **115**(4), pp. 1747–1759.

[26]   Khosla, S., Murugappan, S., and Gutmark, E., 2008, "What can vortices tell us about vocal fold vibration and voice production.," Curr. Opin. Otolaryngol. Head Neck Surg., **16**(3), pp. 183–187.

[27]   Luo, H., Mittal, R., Zheng, X., Bielamowicz, S. A., Walsh, R. J., and Hahn, J. K., 2008, "An immersed-boundary method for flow-structure interaction in biological systems with application to phonation.," J. Comput. Phys., **227**(22), pp. 9303–9332.

[28]   Luo, H., Mittal, R., and Bielamowicz, S. a, 2009, "Analysis of flow-structure interaction in the larynx during phonation using an immersed-boundary method.," J. Acoust. Soc. Am., **126**(2), pp. 816–824.

[29] Zheng, X., Xue, Q., Mittal, R., and Beilamowicz, S., 2010, "A coupled sharp-interface immersed boundary-finite-element method for flow-structure interaction with application to human phonation.," J. Biomech. Eng., **132**(11), p. 111003.

[30] Thomson, S. L., Mongeau, L., and Frankel, S. H., 2005, "Aerodynamic transfer of energy to the vocal folds," J. Acoust. Soc. Am., **118**(3), p. 1689.

[31] Cook, D. D., and Mongeau, L., 2007, "Sensitivity of a continuum vocal fold model to geometric parameters, constraints, and boundary conditions," J. Acoust. Soc. Am., **121**(4), pp. 2247–2253.

[32] Xue, Q., Zheng, X., Mittal, R., and Bielamowicz, S., 2014, "Subject-specific computational modeling of human phonation.," J. Acoust. Soc. Am., **135**(3), pp. 1445–1456.

[33] Mittal, R., Zheng, X., Bhardwaj, R., Seo, J. H., Xue, Q., and Bielamowicz, S., 2011, "Toward a simulation-based tool for the treatment of vocal fold paralysis," Front. Physiol., **MAY**.

[34] Alipour, F., Brucker, C., D. Cook, D., Gommel, A., Kaltenbacher, M., Mattheus, W., Mongeau, L., Nauman, E., Schwarze, R., Tokuda, I., and Zorner, S., 2011, "Mathematical Models and Numerical Schemes for the Simulation of Human Phonation," Curr. Bioinform., **6**(3), pp. 323–343.

[35] Mittal, R., Erath, B. D., and Plesniak, M. W., 2012, "Fluid Dynamics of Human Phonation and Speech," Annu. Rev. Fluid Mech., **45**(1), p. 121008173322000.

[36] Zhang, K., Siegmund, T., and Chan, R. W., 2006, "A constitutive model of the human vocal fold cover for fundamental frequency regulation.," J. Acoust. Soc. Am., **119**(2), pp. 1050–1062.

[37] Zhang, K., Siegmund, T., and Chan, R. W., 2009, "Modeling of the transient responses of the vocal fold lamina propria," J. Mech. Behav. Biomed. Mater., **2**(1), pp. 93–104.

[38] Kelleher, J. E., Siegmund, T., Chan, R. W., and Henslee, E. A., 2011, "Optical measurements of vocal fold tensile properties: Implications for phonatory mechanics," J. Biomech., **44**(9), pp. 1729–1734.

[39] Pickup, B. A., and Thomson, S. L., 2011, "Identification of geometric parameters influencing the flow-induced vibration of a two-layer self-oscillating computational vocal fold model.," J. Acoust. Soc. Am., **129**(4), pp. 2121–32.

[40] Smith, S. L., and Thomson, S. L., 2012, "Effect of inferior surface angle on the self-oscillation of a computational vocal fold model," J. Acoust. Soc. Am., **131**(5), p. 4062.

[41] Chan, R. W., Siegmund, T., and Zhang, K., 2009, "Biomechanics of fundamental frequency regulation: Constitutive modeling of the vocal fold lamina propria," Logop. Phoniatr. Vocology, **34**(4), pp. 181–189.

[42]   Doyle, J. F., 2013, Nonlinear analysis of thin-walled structures: statics, dynamics, and stability, Springer Science & Business Media.

[43]   Tao, C., Jiang, J. J., and Zhang, Y., 2006, "Simulation of vocal fold impact pressures with a self-oscillating finite-element model.," J. Acoust. Soc. Am., **119**(6), pp. 3987–3994.

[44]   Goldsmith, W., 2011, Impact: The Theory and Physical Behavior of Colliding Solids, Dover, New York.

[45]   Decker, G. Z., and Thomson, S. L., 2007, "Computational Simulations of Vocal Fold Vibration: Bernoulli Versus Navier-Stokes," J. Voice, **21**(3), pp. 273–284.

[46]   Titze, I. R., 1994, "Mechanical stress in phonation.," J. Voice, **8**(2), pp. 99–105.

[47]   Isshiki, N., 1998, "Mechanical and dynamic aspects of voice production as related to voice therapy and phonosurgery," J. Voice, **12**(2), pp. 125–137.

[48]   Isshiki N, Morita H, Okamura H, H. M., 1974, "Thyroplasty as a new phonosurgical technique," Acta Otolaryngol, **78**(5–6), pp. 451–457.

[49]   Neumann, K., and Welzel, C., 2004, "The importance of the voice in male-to-female transsexualism," J. Voice, **18**(1), pp. 153–167.

[50]   Gibbins, N., Bray, D., and Harries, M. L., 2011, "Long-term quantitative results of an Isshiki type 4 thyroplasty-a case study," J Voice, **25**(3), pp. 283–287.

[51]   Czerwonka, L., Ford, C. N., Machi, A. T., Leverson, G. E., and Jiang, J. J., 2009, "A-P positioning of medialization thyroplasty in an excised larynx model," Laryngoscope, **119**(3), pp. 591–596.

[52]   Pieter Noordzij, J., Perrault, D. F., Woo, P., Noordzij, J. P., Perrault, D. F., and Woo, P., 1998, "Biomechanics of arytenoid adduction surgery in an ex vivo canine model," Ann. Otol. Rhinol. Laryngol., **107**(6), pp. 454–461.

[53]   Inagi, K., Connor, N. P., Suzuki, T., Ford, C. N., Bless, D. M., and Nakajima, M., 2002, "Glottal configuration, acoustic, and aerodynamic changes induced by variation in suture direction in arytenoid adduction procedures.," Ann. Otol. Rhinol. Laryngol., **111**(10), pp. 861–870.

[54]   Hoffman, M. R., Witt, R. E., Chapin, W. J., McCulloch, T. M., and Jiang, J. J., 2010, "Multiparameter comparison of injection laryngoplasty, medialization laryngoplasty, and arytenoid adduction in an excised larynx model.," Laryngoscope, **120**(4), pp. 769–76.

[55]   Alipour F, F. E., 2013, "On the acoustic effects of the supraglottic structures in excised larynges," J. Acoust. Soc. Am, **133**(5), pp. 2984–2992.

[56]   Alipour, F., and Karnell, M., 2014, "Aerodynamic and acoustic effects of ventricular gap.," J. Voice, **28**(2), pp. 154–60.

[57] Khosla S, Murugappan S, Lakhamraju R, G. E., 2008, "Using particle imaging velocimetry to measure anterior-posterior velocity gradients in the excised canine larynx model," Ann. Otol. Rhinol. Laryngol., **117**(2), pp. 134–144.

[58] Alipour, F., Jaiswal, S., and Finnegan, E., 2007, "Aerodynamic and acoustic effects of false vocal folds and epiglottis in excised larynx models," Ann. Otol. Rhinol. Laryngol., **116**(2), pp. 135–144.

[59] Gray, S., and Titze, I., 1988, "Histologic investigation of hyperphonated canine vocal cords," Ann. Otol. Rhinol. Laryngol., **97**(4 Pt 1), pp. 381–388.

[60] Kojima, T., Van Deusen, M., Jerome, W. G., Garrett, C. G., Sivasankar, M. P., Novaleski, C. K., and Rousseau, B., 2014, "Quantification of acute vocal fold epithelial surface damage with increasing time and magnitude doses of vibration exposure," PLoS One, **9**(3), p. e91615.

[61] Kojima, T., Valenzuela, C. V., Novaleski, C. K., Van Deusen, M., Mitchell, J. R., Garrett, C. G., Sivasankar, M. P., and Rousseau, B., 2014, "Effects of phonation time and magnitude dose on vocal fold epithelial genes, barrier integrity, and function," Laryngoscope, **124**(12), pp. 2770–2778.

[62] Awan, S. N., Novaleski, C. K., and Rousseau, B., 2014, "Nonlinear Analyses of Elicited Modal, Raised, and Pressed Rabbit Phonation," J. Voice, **28**(5), pp. 538–547.

[63] M., H., 1974, "morphological structure of the vocal cord as a vibrator and its variations," Folia Phoniatr. (Basel), **26**(2), pp. 89–94.

[64] Khosla, S., Muruguppan, S., Gutmark, E., and Scherer, R., 2007, "Vortical flow field during phonation in an excised canine larynx model.," Ann. Otol. Rhinol. Laryngol., **116**(3), pp. 217–228.

[65] Bakhshaee, H., Young, J., Yang, J. C., Mongeau, L., and Miri, A. K., 2013, "Determination of Strain Field on the Superior Surface of Excised Larynx Vocal Folds Using DIC," J. Voice, **27**(6), pp. 659–667.

[66] J., V. den B., 1958, "Myoelastic-aerodynamic theory of voice production," J. Speech Hear. Res., **1**(3), pp. 227–244.

[67] Chang, S., Tian, F.-B., Luo, H., Doyle, J. F., and Rousseau, B., 2013, "The role of finite displacements in vocal fold modeling.," J. Biomech. Eng., **135**(11), p. 111008.

[68] Ge, P. J., French, L. C., Ohno, T., Zealear, D. L., and Rousseau, B., 2009, "Model of evoked rabbit phonation," Ann. Otol. Rhinol. Laryngol., **118**(1), pp. 51–55.

[69] Titze, I. R., 1988, "The physics of small-amplitude oscillation of the vocal folds.," J. Acoust. Soc. Am., **83**(4), pp. 1536–1552.

[70] Zhang, Y., and Jiang, J. J., 2004, "Chaotic vibrations of a vocal fold model with a

unilateral polyp.," J. Acoust. Soc. Am., **115**(3), pp. 1266–1269.

[71] Zheng, X., and Mittal, R., 2011, "A computational study of asymmetric glottal jet deflection during phonation," **129**(April), pp. 2133–2143.

[72] Tian, F.-B., Dai, H., Luo, H., Doyle, J. F., and Rousseau, B., 2014, "Fluid-structure interaction involving large deformations: 3D simulations and applications to biological systems.," J. Comput. Phys., **258**, pp. 451–469.

[73] Tao, C., and Jiang, J. J., 2007, "Mechanical stress during phonation in a self-oscillating finite-element vocal fold model," J. Biomech., **40**(10), pp. 2191–2198.

[74] Swanson, E. R., Ohno, T., Abdollahian, D., Garrett, C. G., and Rousseau, B., 2010, "Effects of raised-intensity phonation on inflammatory mediator gene expression in normal rabbit vocal fold," Otolaryngol. - Head Neck Surg., **143**(4), pp. 567–572.

[75] Novaleski, C. K., Kojima, T., Chang, S., Luo, H., Valenzuela, C. V., and Rousseau, B., "Non-stimulated rabbit phonation model: Cricothyroid approximation," Laryngoscope (In Press.

[76] Zhang, Z., 2009, "Characteristics of phonation onset in a two-layer vocal fold model.," J. Acoust. Soc. Am., **125**(2), pp. 1091–1102.

[77] Thibeault, S. L., Gray, S. D., Bless, D. M., Chan, R. W., and Ford, C. N., 2002, "Histologic and rheologic characterization of vocal fold scarring," J. Voice, **16**(1), pp. 96–104.

[78] Rousseau, B., Hirano, S., Chan, R. W., Welham, N. V., Thibeault, S. L., Ford, C. N., and Bless, D. M., 2004, "Characterization of chronic vocal fold scarringin a rabbit model," J. Voice, **18**(1), pp. 116–124.

[79] Latifi, N., Miri, A. K., and Mongeau, L., 2014, "Determination of the elastic properties of rabbit vocal fold tissue using uniaxial tensile testing and a tailored finite element model," J. Mech. Behav. Biomed. Mater., **39**, pp. 366–374.

[80] Miller, K., 2001, "How to test very soft biological tissues in extension?," J. Biomech., **34**(5), pp. 651–657.

[81] Mooney, M., 1940, "A theory of large elastic deformation," J. Appl. Phys., **11**(9), pp. 582–592.

[82] Tian, F.-B., Dai, H., Luo, H., Doyle, J. F., and Rousseau, B., 2014, "Fluid-structure interaction involving large deformations: 3D simulations and applications to biological systems.," J. Comput. Phys., **258**, pp. 451–469.

[83] Titze, I. R., Jiang, J. J., and Hsiao, T. Y., 1993, "Measurement of mucosal wave propagation and vertical phase difference in vocal fold vibration," Ann. Otol. Rhinol. Laryngol., **102**(1 I), pp. 58–63.

[84] Baken, R. J., and Orlinkoff, R. F., 2000, Clinical measurement of speech and voice.